Astronomy & Astrophysics manuscript no. 37498corr
February 21, 2020

Luminosity calculation of meteor entry based on detailed flow simulations in the continuum regime

B. Dias[1,2,⋆], J.B. Scoggins[1,3], and T. E. Magin[1]

[1] von Karman Institute for Fluid Dynamics, Waterloosesteenweg 72, 1640 St.-Genesius-Rode, Belgium
[2] Université Catholique de Louvain, Institute of Mechanics, Materials and Civil Engineering, Place du Levant 2, 1348 Louvain-la-Neuve, Belgium
[3] CMAP, École Polytechnique, Route de Saclay, Palaiseau 91128, France

Received January 12 2020; accepted February 17 2020

ABSTRACT

Context. Composition, mass, and trajectory parameters of meteors can be derived by combining observations with the meteor physics equations. The fidelity of these equations, which rely on heuristic coefficients, significantly affects the accuracy of the properties inferred.

Aims. Our objective is to present a methodology that can be used to compute the luminosity of meteor entry based on detailed flow simulations in the continuum regime.

Methods. The methodology consists in solving the Navier-Stokes equations using state-of-the-art physico-chemical models for hypersonic flows. It includes accurate boundary conditions to simulate the surface evaporation of the molten material and coupled flow-radiation effects. Such detailed simulations allow for the calculation of heat-transfer coefficients and luminous efficiency, which can be incorporated into the meteor physics equations. Finally, we integrate the radiative transfer equation over a line of sight from the ground to the meteor to derive the luminosity magnitude.

Results. We use the developed methodology to simulate the Lost City bolide and to derive the luminosity magnitude, obtaining good agreement between numerical results and observations. The computed color index is more prominent than the observations. This is attributed to a lack of refractory elements such as Ca in the modeled flow that might originate from the vaporization of droplets in the trail, a phenomenon currently not included in the model.

Key words. Meteorites, meteors, meteoroids - shock waves -methods:numerical - Radiation mechanisms: thermal

1. Introduction

The meteoroid mass influx is a quantity of interest for several fields, such as aeronomy, planetary science, and astrobiology (Jenniskens et al. 1998). Even though there is a worldwide effort to detect meteors (Borovička et al. 1999; Lamy et al. 2011; Weryk et al. 2013; Howie et al. 2017), the amount of meteoroid mass entering planet Earth is quite uncertain. This uncertainty is greatly affected by the inaccuracy of the meteor physics equations used to derive composition, mass, and trajectory parameters of each incoming object. These equations written in an ordinary differential form, also known as the single body theory, go back to the work of Öpik (1958) from a time in which the computational resources to solve such a phenomenon were limited; today this remains a colossal task. The model contains heuristic coefficients, such as the heat-transfer and luminous efficiency (part of the kinetic energy which is transformed into light), which are very often correlated to meteor observations (McCrosky & Ceplecha 1970).

Several authors have previously combined photographic observations with an extension of the single body theory, including fragmentation (Baldwin & Sheaffer 1971), to derive the mass and the trajectory of meteoroids by obtaining the best fit for heuristic coefficients. For example, Gritsevich & Koschny (2011) combined photometric with dynamical measurements from several observations to constrain the luminous efficiency. Among several observations, the Lost City bolide (McCrosky et al. 1971) is one of the first well-documented events from which light magnitude and trajectory were measured. This bolide serves as a reference to derive heuristic coefficients, and ReVelle & Rajan (1979) sought the opportunity to derive the luminous efficiency and photographic mass from these observations, disregarding fragmentation. Years later, Ceplecha (1996) used the same observations and improved the inference of the luminous efficiency and the photographic mass by including a gross-fragmentation model. Ceplecha & ReVelle (2005) generalized the definition of luminous efficiency as a function of mass, velocity, and normalized air density. These latter authors obtained this intrinsic luminous efficiency by calibrating their fragmentation model with the best observational fit of Lost City bolide. This work represented a breakthrough in the definition of the luminous efficiency because it is typically assumed that this parameter depends only on the velocity (Verniani 1965). More recently, Subasinghe & Campbell-Brown (2018) inferred the luminous efficiency from 15 meteoroids and showed that this parameter does not depend only on the velocity.

The meteoroid composition greatly affects the intensity of the meteor luminosity. Due to spectral measurements of several meteors (Borovička 1993; Madiedo et al. 2013a,b), astronomers are now able to catalog the composition of different meteor showers and infer their origin (Vojáček et al. 2015). Moreover, Borovička & Betlem (1997) derived the luminous efficiency from the classical luminosity equation by analyzing the spec-

---

[⋆] Corresponding author, e-mail: `barros@vki.ac.be`

Article published by EDP Sciences, to be cited as https://doi.org/10.1051/0004-6361/202037498

tra of two meteors from the Perseid shower. From the spectra, Borovička & Betlem (1997) and Borovička & Berezhnoy (2016) were able to identify the temperature of each chemical species assuming radiative equilibrium conditions, distinguishing two different regions; a vapor layer region containing species with a temperature below 5000 K (mainly evaporation components also referred to as the main spectrum), and the shock layer region where the species have temperatures above 10000 K (known as the second spectrum containing mainly N and O from the shock layer).

One of the major drawbacks of the meteor physics equations is the lack of detailed physico-chemical modeling, which is fundamental to simulate hypersonic entries. For example, these equations do not account for the thermodynamic and chemical nonequilibrium across the shock and the boundary layer (Gnoffo et al. 1989). Moreover, the radiative effects on the shock layer are also not considered. Ceplecha et al. (2000) mentions this lack of fidelity by showing some trajectories that cannot be explained with these equations alone. Furthermore, (Ceplecha & ReVelle 2005) suggest that the meteor physics equations may require improvements. The entry of meteoroids is complex and therefore difficult to model because it involves numerous physical phenomena in the shock layer and the multiphase physics that the material endures, involving melting and evaporation. Moreover, during the flight, the meteoroid spans a wide range of flow conditions, from free-molecular and rarefied effects to the continuum regime. For smaller meteoroids at high altitude, where the Kn number is high and the flow is under rarefied conditions, the interested reader is directed to the works of Boyd (2000), Jenniskens (2004), and Bariselli et al. (2019).

In the last twenty years, several authors have been concerned by developing models to include detailed flow, radiation, and ablation coupling effects in the continuum regime. Within these models, there are two types of approach: The first involves inviscid simulations which are fast and relatively easy to solve, but the dissipation terms in the boundary layer are neglected, which influences the evaporation boundary condition. The second involves viscous simulations which resolve the boundary layer but in turn are harder to solve and are computationally expensive for multidimensional cases. Park (2013, 2014, 2015) performed coupled ablation radiation simulations assuming an inviscid flow field in thermal-equilibrium conditions. The incoming air layer and ablation layer divided the inviscid shock layer in two flow regions, and approximate methods are used to simulate them. Moreover, these latter authors modeled the radiative transfer with the Rosseland approximation, which is only valid for optically thick systems. Golub et al. (1996) derived heat-transfer and luminous efficiency, assuming an inviscid flow, but in turn included thermal nonequilibrium effects. These latter authors modeled the ablation products as a 1D cylindrical piston plunging into a quasi-stationary hypersonic flow, assuming no mixing between the two layers. Svettsov et al. (2018) computed the radiative field of Chelyabinsk using the Rosseland approximation. The body was treated as a liquid-like strengthless object (Shuvalov & Artemieva 2002) due to a lack of solidity at low altitude. Shuvalov & Artemieva (2002) computed the effects of radiation felt on Earth's surface by solving the radiative transfer equation assuming an inviscid, thermal-equilibrium flow around the body.

Silber et al. (2017) solved the flow field with the Navier-Stokes equations via computational methods. These latter authors studied the chemical kinetics on the trail of a nonablating small meteoroid at high altitude. Even though the objective of their work was to study reaction rates during a meteoroid entry, it lacks fundamental thermodynamic and transport properties at high temperatures, which might result in an erroneous interpretation of the chemical kinetics. To date, Johnston et al. (2018) showed one of the highest fidelity models on the coupling of flow, ablation, and radiation for meteoroid entries. In that work, the authors derived heat-transfer coefficients for Chelyabinsk-type bolides; even though they use state-of-the-art physico-chemical models to treat hypersonic flows, the surface evaporation is considered to be in equilibrium. The equilibrium boundary condition might be a strong assumption for these flow conditions because the nonequilibrium effects become more predominant for massive ablation rates. Moreover, with their boundary condition, it is not possible to solve the evaporation of volatiles. The extraction of the meteoroid physical parameters from observations requires strong assumptions of the flow physics, such as the flow being in local thermo-chemical equilibrium conditions. The most systematic approach is to compare the observations with 3D computational fluid dynamic (CFD) simulations, which are computationally expensive for the flow in question.

The objective of this paper is to present a methodology (Sec. 2) to simulate the entry of meteoroids using state-of-the-art physico-chemical models with a quasi-1D approach. This methodology includes accurate boundary conditions to simulate the evaporation of the meteoroid and coupled flow–radiation effects. Detailed simulations allow for the calculation of heat-transfer coefficients and luminous efficiency. We focus on meteoroids that are within the continuum assumption; thus, their flow field can be solved by means of the Navier-Stokes equations. Moreover, we make no assumptions on the thermodynamic and chemical state of the flow. In contrast, we assume a nonfragmenting body with a perfectly spherical shape, and we only model the plasma flow around the main body. The study of the meteor trail is beyond the scope of this paper. From the detailed flow and radiative fields, we compute the heat-transfer coefficient and luminous efficiency for an H5 chondrite and an iron meteoroid (Sec. 3.1) that can be used in the heuristic models. Finally, we compare the absolute magnitude of Lost City bolide with observations (Sec. 3.2) shown by Ceplecha & ReVelle (2005). One original contribution of our work is to use high-fidelity models to compute the absolute light magnitude and to compare with observations without the complexity of multi-dimensional simulations.

2. Methodology

In this section, we describe the Navier-Stokes equations for hypersonic flows and their closure using state-of-art physico-chemical models. We consider a two-temperature model (Park 1988, 1989) to describe the thermal state of the flow. This model assumes that the translational mode of the heavy species and rotational mode of molecules follows a Boltzmann distribution at temperature T whereas the vibrational mode of molecules, the electronic mode of heavy species, and the translational mode of the free electron follow a Boltzmann distribution at temperature T^{ve}. Chemical and energy source terms due to radiation are included in the Navier-Stokes equations by following the work of Soucasse et al. (2016). We update the database of atomic lines and photoionization to include material ablation products. The boundary conditions of the governing equations are obtained by solving mass and energy fluxes at the surface, including the Hertz-Knudsen law for evaporation. Within this methodology, we derive the heat-transfer coefficient and the luminous efficiency from detailed simulations.

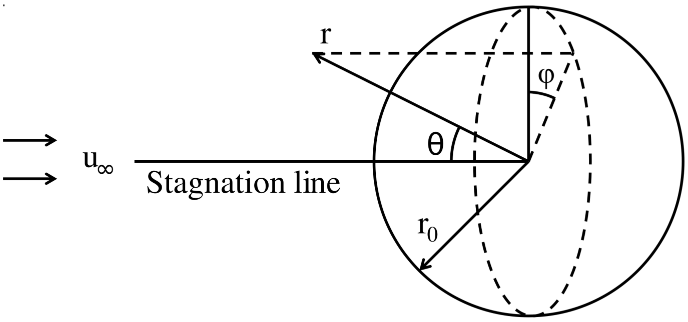

Fig. 1: Spherical body of radius r_0 subjected to a hypersonic flow at u_∞. Azimuth and zenith angles are φ and θ, respectively.

2.1. Stagnation line flow

We simulate the hypersonic flow around spherical bodies using a reduced form of the 2D axisymmetric Navier-Stokes equations to a quasi-1D approximation for the stagnation streamline (Klomfass & Muller 2000). This reduction was achieved by using the following similarity transformation:

$$T = \overline{T}(r), \quad T^{ve} = \overline{T}^{ve}(r), \quad y_i = \overline{y}_i(r) \quad \forall i \in \mathcal{S}, \tag{1}$$

where the temperatures and mass fraction y_i of species i in the set of species $\mathcal{S}$ depend only on the radial coordinate r, while the radial and azimuthal velocity components and the mixture pressure p and electron pressure p_e depend also on the polar angle θ such as:

$$\begin{aligned} u_r &= \overline{u}_r(r) cos\ \theta, & u_\theta &= \overline{u}_\theta(r) sin\ \theta, \\ p - p_\infty &= \overline{p}(r) cos^2\ \theta, & p_e - p_{e,\infty} &= \overline{p}_e(r) cos^2\ \theta. \end{aligned} \tag{2}$$

Taking the limit $\theta \to 0$, the stagnation streamline formulation referred to as the dimensionally reduced Navier Stokes equations (DRNSE), are written as

$$\frac{\partial}{\partial t}\mathbf{U} + \frac{\partial}{\partial r}\mathbf{F^{inv}} + \frac{\partial}{\partial r}\mathbf{F^{vis}} = \mathbf{S^{inv}} + \mathbf{S^{vis}} + \mathbf{S^{kin}} + \mathbf{S^{rad}}, \tag{3}$$

where the vector $\mathbf{U}$ denotes the volume-specific balance quantities, $\mathbf{F^{inv}}$ are the inviscid fluxes, and $\mathbf{F^{vis}}$ are the viscous terms. Vectors $\mathbf{S^{kin}}$ and the $\mathbf{S^{rad}}$ are the kinetic and the radiative source terms, while $\mathbf{S^{inv}}$ and $\mathbf{S^{vis}}$ are the inviscid and viscous source terms arising from the DRNSE transformation.

For the two-temperature model of Gnoffo et al. (1989), this yields Soucasse et al. (2016):

$$\mathbf{U} = \left[\rho_i,\ \rho u_r,\ \rho u_\theta,\ \rho E,\ \rho e^{ve}\right]^T,$$

$$\mathbf{F^{inv}} = \left[\rho_i u_r,\ \rho u_r^2 + p,\ \rho u_r u_\theta,\ \rho u_r H,\ \rho u_r e^{ve}\right]^T,$$

$$\mathbf{F^{vis}} = \left[\mathrm{J}_{ri},\ -\tau_{rr},\ -\tau_{r\theta},\ q_r - \tau_{rr}u_r,\ q_r^{ve}\right]^T,$$

$$\mathbf{S^{inv}} = -\frac{(u_r + u_\theta)}{r}\Big[2\rho_i,\ 2\rho u_r,\ 3\rho u_\theta - 2\frac{p - p_\infty}{u_r + u_\theta},$$
$$2\rho H, 2\rho e^{ve}\Big]^T,$$

$$\mathbf{S^{vis}} = -\frac{1}{r}\Big[2\mathrm{J}_{ri},\ 2(\tau_{\theta\theta} - \tau_{rr} + \tau_{r\theta}),$$
$$\tau_{\theta\theta} - 3\tau_{r\theta},\ 2(q_r - \tau_{rr}u_r - \tau_{\theta\theta}u_r - \tau_{r\theta}u_\theta),\ 2q_r^{ve}\Big]^T,$$

$$\mathbf{S^{kin}} = \left[\dot{\omega}_i^{chem},\ 0,\ 0,\ 0,\ \Omega^{ve}\right]^T,$$

$$\mathbf{S^{rad}} = \left[\dot{\omega}_i^{rad},\ 0,\ 0,\ \mathcal{P}^{rad},\ \mathcal{P}^{rad,ve}\right]^T,$$

where the total energy per unit volume is written as $\rho E = \rho e + \rho u_r^2/2$ with ρ being the mixture mass density. The total enthalpy is given as $H = E + p/\rho$. The total internal energy of the mixture is defined as:

$$\rho e = \sum_{i\in\mathcal{H}} \rho_i e_i(T, T^{ve}) + \rho_e e_e^T(T^{ve}),$$

where ρ_e and e_e^T are respectively the electron density and the electron internal energy. The internal energy for the heavy species $\mathcal{H}$ is defined as:

$$\begin{cases} e_i^T(T) + e_i^E(T^{ve}) + e_i^F, & \forall i \in \mathcal{A}, \\ e_i^T(T) + e_i^R(T) + e_i^V(T^{ve}) + e_i^E(T^{ve}) + e_i^F, & \forall i \in \mathcal{M}, \end{cases}$$

where the superscript $T, V, R,$ and E represent the translational, vibrational, rotation, and electronic modes, $\mathcal{A}$ represents the set of atoms, and $\mathcal{M}$ is the set of molecules. The term e_i^F represents the formation energy of the species i at 298 K. The pressure is retrieved with the perfect gas law as $p = \sum_{i\in\mathcal{H}} \rho_i R_i T + \rho_e R_e T^{ve}$, where R_i is the perfect gas constant of the species i. The total and internal heat flux on the radial direction read as:

$$q_r = \sum_{i\in\mathcal{S}} J_{r,i}h_i - \lambda^T\frac{\partial T}{\partial r} - \lambda^{ve}\frac{\partial T^{ve}}{\partial r}, \tag{4}$$

$$q_r^{ve} = \sum_{i\in\mathcal{S}} J_{r,i}h_i^{ve} - \lambda^{ve}\frac{\partial T^{ve}}{\partial r}, \tag{5}$$

where the set $\mathcal{S}$ comprises all the species, $J_{r,i}$ corresponds to the diffusion flux of species i (obtained by solving the Stefan-Maxwell system Magin (2004)), and λ^T and λ^{ve} are the thermal conductivities of the translation and internal modes, respectively. The different components of the viscous stress tensor read as:

$$\tau_{rr} = \frac{4}{3}\mu\left(\frac{\partial u_r}{\partial r} - \frac{u_r + u_\theta}{r}\right), \tag{6}$$

$$\tau_{r\theta} = \mu\left(\frac{\partial u_\theta}{\partial r} - \frac{u_r + u_\theta}{r}\right), \tag{7}$$

$$\tau_{\theta\theta} = -\frac{1}{2}\tau_{rr}, \tag{8}$$

where μ corresponds to the viscosity.

From the law of mass action, the chemical production rate

$$\dot{\omega}_i^{chem} = M_i\sum_{r\in\mathcal{R}} \nu_{ir}\Re_r, \tag{9}$$

where $\nu_{ir} = \nu_{ir}^{''} - \nu_{ir}^{'}$ and the symbol M_i stands for the species molar mass.

The rate of progress for reaction r is given by

$$\Re_r = k_r^f\prod_{i\in\mathcal{S}}\left(\frac{\rho_i}{M_i}\right)^{\nu_{ir}^{'}} - k_r^b\prod_{i\in\mathcal{S}}\left(\frac{\rho_i}{M_i}\right)^{\nu_{ir}^{''}}, \quad \forall r \in \mathcal{R},$$

for a system of reactions $r \in \mathcal{R}$ such that

$$\sum_{i\in\mathcal{S}} \nu_{ir}^{'}X_i \rightleftharpoons \sum_{i\in\mathcal{S}} \nu_{ir}^{''}X_i,$$

where X_i is the chemical symbol for species $i \in \mathcal{S}$, and $\nu_{ir}^{'}$ and $\nu_{ir}^{''}$ are the forward and backward stoichiometric coefficients for species i in reaction r. The forward rate k_r^f follows an Arrhenius-type law given by Tab. B.1 and the backward rate is evaluated as

$k_r^b = k_r^f(T_r^b)/K_{\mathrm{eq},r}(T_r^b)$, where K_{eq} corresponds to the equilibrium constant of the reaction r.

The energy transfer due to collisions between the translation–rotational and the vibration–electronic–electron modes reads as

$$\Omega^{ve} = -p_e\left(\frac{\partial u_r}{\partial r} + 2\frac{u_r + u_\theta}{r}\right) + \sum_{j\in\mathcal{H}} \rho_j \frac{e_j^v(T) - e_j^v(T^v)}{\tau_j^{VT}} + \sum_{j\in\mathcal{H}} e_j^{V,E}\dot{\omega}_j^{chem} + \rho_e\frac{e_e^T(T) - e_e^T(T_e)}{\tau^{eT}} + \sum_{r\in\mathcal{I}} \Delta H^r \Re_r, \quad (10)$$

where the first term on the right-hand side corresponds to internal work done by the electron pressure, and the second term is the vibration-translation energy exchange where τ_j^{VT} corresponds to the Millikan & White (1963) relaxation time with the Park (1993) correction for high-temperature flows. The third term corresponds to the energy added to the vibration-electronic mode due to chemical reactions. The fourth term corresponds to the energy transfer due to elastic collisions between the free electron and the heavy particle; the relaxation time τ^{eT}. Finally, the last term corresponds to the energy provided by the electron bath during electron-impact ionization of reactions $\mathcal{I}$. The term ΔH^r corresponds to the necessary energy to ionize an atom from its ground state. Hartung et al. (1992) suggest taking the ionization energy for the electron-impact ionization reactions of N and O from an excited state; therefore, we use $4.05 \times 10^8 \mathrm{J\,kg^{-1}\,mol^{-1}}$ for the reaction (29) and $4.3 \times 10^8 \mathrm{J\,kg^{-1}\,mol^{-1}}$ for the reaction (30) of Tab. B.1.

Photochemical mass production rate of species i, $\dot{\omega}_i^{rad}$ represents the creation or destruction of species i during bound-free radiative processes, such as photoionization ($A + hc\sigma \rightleftharpoons A^+ + e^-$) or photodissociation ($AB + hc\sigma \rightleftharpoons A + B$). The radiative powers $\mathcal{P}^{rad}$ and $\mathcal{P}^{rad,ve}$ represent the energy source terms due to radiative processes that contribute to the total energy and the vibronic modes, respectively. The total radiative source term is given as the negative divergence of the radiative heat flux, q^{rad},

$$\mathcal{P}^{rad}(r) = -\frac{\partial}{\partial r}q^{rad}(r). \quad (11)$$

The vibronic radiative energy source term is estimated by neglecting radiative energy exchanges with translational and rotational modes. In particular, we assume

$$\mathcal{P}^{rad,ve}(r) = \mathcal{P}^{rad}(r) - \sum_{p\in\mathcal{J}} \Delta h_p \dot{\omega}_{p,e}^{rad}(r) - \mathcal{P}_{\mathrm{SR}}^{rad} + \dot{\omega}_{\mathrm{SR}}^{rad}(E_{\mathrm{O^1D}}^{\mathrm{el}} - \bar{E}_{\mathrm{O_2}}^{\mathrm{vib}}), \quad (12)$$

where $\mathcal{J}$ is the set of photoionization processes, $\dot{\omega}_{p,e}^{rad}$ is the electron mass production rate for the bound-free process p, and Δh_p is the ionization energy per unit mass of the electron. The terms $\mathcal{P}_{\mathrm{SR}}^{rad}$ and $\dot{\omega}_{\mathrm{SR}}^{rad}$ are the radiative power and production rate of O^1D, respectively, associated with the Schumann-Runge photodissociation process, $O_2(X) + hc\sigma \rightleftharpoons O^3P + O^1D$. Finally, $E_{\mathrm{O^1D}}^{\mathrm{el}}$ and $\bar{E}_{\mathrm{O_2}}^{\mathrm{vib}}$ are the electronic energy of the first excited state of atomic oxygen and the average vibrational energy of the ground electronic state of O_2, respectively. The summation on the right-hand side accounts for the part of the photon energy transformed into formation energy during photoionization processes (Lopez et al. 2013), while the remaining terms account for the formation and translational energy production due to the Schumann-Runge O_2-photodissociation. To our knowledge, these last terms are a novel contribution; they proved to be crucial for the stability of the numeric solver when significant photodissociation occurs in front of the shock. The radiative source terms and heat flux are computed using the Hybrid Statistical Narrow Band (HSNB) Model (Lamet et al. 2010), coupled with a 1D tangent slab approximation, as explained in (Soucasse et al. 2016). The HSNB model is a hybrid spectral reduction approach in which optically thick molecular systems are modeled using a statistical narrow-band model, optically thin molecules, and continuum processes are computed using a Box model. Atomic lines are computed with a line-by-line (LBL) approach. The interested reader is directed to the work of Soucasse et al. (2016) for further details. We include the Na, Na^+, Ca, Si, Fe, Fe^+, Mg and Mg^+ bound-bound radiative transitions from the Nist database (Kramida & Ralchenko 1999) and the theoretical absorption cross-sections of Na for the bound-free processes were taken from TOPbase (Cunto et al. 1993).

Table 1: Gaseous species used in this work. The evaporation products contain only the major species according to their saturated vapor pressure.

air species
e^- N NO N_2 O O_2 N^+ O^+ NO^+ N_2^+ O_2^+
H5 chondrite evaporation products
Mg Mg^+ MgO FeO Si SiO SiO_2 Na Na^+ NaO K Fe Fe^+
iron meteoroid evaporation products
Fe Fe^+

The open-source library Mutation++[1] (Scoggins et al. 2020) provided the necessary thermodynamic, transport, and kinetic properties used in this work. The full set of species considered is listed in Tab. 1. When necessary, additional data have been added to the Mutation++ database for the thermodynamic, transport, and chemical kinetic properties (see Appendix B for more details).

Equation 3 is discretized in space with the finite-volume method (Munafò & Magin 2014). We compute the convective fluxes at the interface with the AUSM+-up2 scheme by Kitamura & Shima (2013), and we impose the boundary conditions through ghost-cells. The time derivatives are computed with the Backward-Euler method, and the solution is obtained once the flow reaches a steady state.

2.2. Gas–surface interaction

The evaporation composition $y_{i,w}$, and the surface temperature T_w are the solutions of a nonlinear system of mass and energy balance at the surface. These properties are boundary conditions of the flow governing equations. The surface mass balance (SMB) is expressed as,

$$J_{i,w} + \dot{m}_{\mathrm{vap},i} = (\rho v)_w y_{i,w}, \quad \forall\ \mathrm{i} \in \mathcal{S}, \quad (13)$$

where $(\rho v)_w$ is the total gas blowing, $\dot{m}_{\mathrm{vap},i}$ is the net evaporation or condensation rate and $J_{i,w}$ is the diffusive flux of the species. The total mass-blowing rate is retrieved by summing Eq. 13 over all species, that is,

$$\sum_{i\in\mathcal{S}} \dot{m}_{\mathrm{vap},i} = \dot{m}_{\mathrm{vap}} = (\rho v)_w, \quad (14)$$

The surface energy balance (SEB) is given in the expression,

$$q_{cond} + \epsilon q_{rad,in} = \epsilon\sigma T_w^4 + \dot{m}_{\mathrm{vap}}\mathrm{L}_{\mathrm{heat}}, \quad (15)$$

---

[1] `https://github.com/mutationpp/Mutationpp`

where the terms on the left side represent the incoming conductive heat flux and the radiative heat flux, which is a result of the radiative transfer equation (RTE) calculation (in this work we use ϵ=0.85). On the right side, the leaving fluxes are the re-radiation of the material and energy lost due to evaporation, where the material's latent heat of evaporation $\mathrm{L_{heat}} = 6.0 \times 10^6 \mathrm{J\,kg^{-1}}$ for the ordinary chondrite (Vondrak et al. 2008) and $\mathrm{L_{heat}} = 6.1 \times 10^6 \mathrm{J\,kg^{-1}}$ for iron meteorites. We do not include the material heat conduction in the energy balance. The inclusion of this term requires a flow–material coupling, which is out of the scope of this paper.

The closure of Eq. 13 is given by the Hertz-Knudsen law,

$$\dot{m}_{\mathrm{vap},i} = \left(\frac{\mathcal{M}_i}{2\pi\mathcal{R}_i T_w}\right)^{\frac{1}{2}} \alpha(p_{\mathrm{vap},i}-p_{w,i}), \quad \forall\ \mathrm{i} \in \mathcal{S}, \tag{16}$$

where we assume the evaporation or condensation coefficient $\alpha = 1$, $p_{w,i}$ corresponds to the species partial pressure at the surface, and the equilibrium vapor pressure, $p_{\mathrm{vap},i}(T_w)$, is computed through the multiphase equilibrium solver Magma (Fegley & Cameron 1987). This quantity has been fitted in the form of,

$$p_{\mathrm{vap},i}(T_w) = \exp\left(A - \frac{B}{T_w}\right), \qquad \forall i \in \mathcal{S},$$

and the coefficients A and B can be found in appendix A.

The oxide composition of the H5 chondrite used as input in Magma is shown in Tab. 2 and the corresponding equilibrium vapor pressure in Fig. 2. The multiphase equilibrium state computed by Magma does not consider the existence of the atmospheric oxygen; therefore, it is not possible to model oxidation or reduction reactions on the surface. In order to be consistent with the reactions present in Magma, the mass flux in Eq. 16 includes all the possible reactions of the type,

$$\mathrm{X_aO_b(l)} \rightleftharpoons \mathrm{a\,X(g)} + \mathrm{b\,O(g)}, \quad \text{and} \tag{17}$$

$$\mathrm{X_aO_b(l)} \rightleftharpoons \mathrm{X_aO_b(g)}, \tag{18}$$

where X represents any evaporation element such as Mg, Fe, Na, Si, and K. The reaction in Eq. 17 is a dissociative reaction, it occurs for species with low dissociation energy. Since oxygen is also present in the free-stream and it is difficult to quantify how much oxygen condensates, the rate of condensation of oxygen is assumed to follow the stoichiometry shown by Eq. 17, as suggested by Alexander (2001), such that,

$$\dot{m}_O = \sum_{r\in\mathcal{R}^\star} \frac{\mathrm{b}}{\mathrm{a}} \frac{\mathrm{M_O}}{\mathrm{M_X}} \dot{m}_{\mathrm{X},r}, \tag{19}$$

where $\mathcal{R}^\star$ corresponds to all reactions of the type of Eq. 17 and $\dot{m}_{\mathrm{X},r}$ is computed via Eq. 16.

2.3. Heat-transfer coefficient and luminous efficiency

This section shows the methodology we develop to derive the heat-transfer coefficient and luminous efficiency from detailed simulations. The heat-transfer coefficient, C_h, indicates the amount of kinetic energy of the meteor that is translated to the surface of the body as heat. From the methodology presented in this paper, we are able to directly estimate the stagnation point heat flux allowing us to define the heat-transfer coefficient as

$$C_h = \frac{q_{conv} + \epsilon q_{rad,in}}{\frac{1}{2}\,\rho_\infty v_\infty^3}. \tag{20}$$

Table 2: Major oxides present in an H5 chondrite in weight percentage, taken from Jarosewich (1990) (the weight fractions are re-scaled here to sum to 100 when removing trace species).

Species	H5 wt%
SiO_2	38.36
TiO_2	0.12
Al_2O_3	2.12
Na_2O	1.03
K_2O	0.13
CaO	1.75
FeO	11.28
MgO	24.22

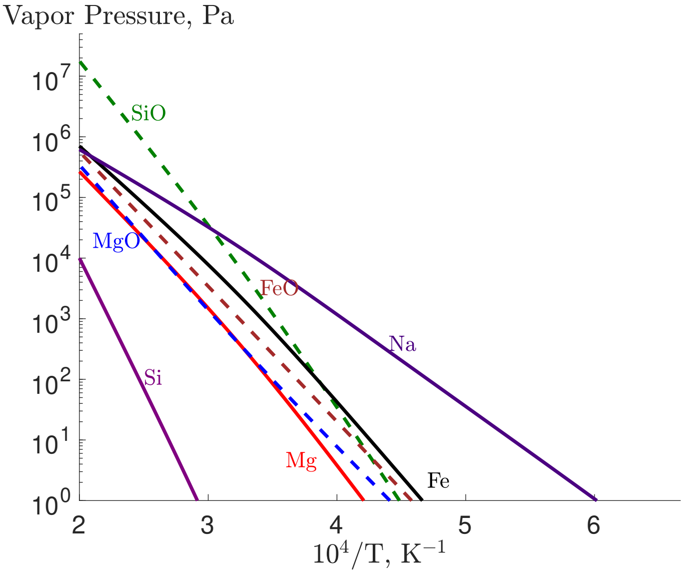

Fig. 2: Saturation vapor pressure computed by Magma using the composition from Tab. 2. The dashed and solid lines represent the products of reactions 17 and 18.

The traditional luminosity equation for a nondecelerating body is given as

$$I_\alpha = \tau_\alpha \frac{v_\infty^2}{2} \frac{dm}{dt}, \quad \forall\ \alpha \in \{T, V, B, R\}, \tag{21}$$

where I_α represents the meteor luminosity and has the units of Watts, τ_α is the unitless luminous efficiency, v_∞ is the bolide velocity, and dm/dt is the mass lost in $\mathrm{kg\,s^{-1}}$ ($dm/dt = \int_A \dot{m}_{\mathrm{vap}}\, dA$, where A is the surface area of the object). The index α in Eq. 21 concerns the luminosity in a specific band, i.e., T represents the total spectrum, V the visible band, B the blue band, and R the red band. The luminous efficiency represents the portion of kinetic energy transformed into radiation (the deceleration is not considered), and more specifically, Eq. 21 assumes that the radiation induced by the emission of the evaporation products and the atmospheric radiative mechanism are negligible (Bronshten 1983).

We write the original definition of the luminosity equation (Ceplecha et al. 1998) to take into account the average quantities from the SNB method (in Appendix A we show the derivation from the original equation):

$$I_\alpha = 4\pi r^2 \sum_{\Delta\sigma} \overline{\alpha_\sigma}^{\Delta\sigma} \overline{I_\sigma}^{\Delta\sigma} \Delta\sigma, \quad \forall\ \alpha \in \{T, V, B, R\}, \tag{22}$$

where $4\pi r^2$ represents the radiative spherical volume. In Eq. 22, $\overline{\alpha_\sigma}^{\Delta\sigma}$ is the UBVRI passband filter (taken from Bessell (1990)) averaged over a narrow band; in the case of $\alpha = T$ then $\overline{T_\sigma}^{\Delta\sigma} = 1$.

The luminosity recorded by any observation device corresponds to the radiative spectral flux from the meteor. Therefore, to represent this spectral flux, we solve the RTE on a line of sight from the meteoroid stagnation point to the ground. Moreover, since the surrounding environment can absorb the luminosity, we include the atmospheric conditions on the RTE integration. The spectral flux is,

$$\overline{F_\sigma}^{\Delta\sigma} = \pi \overline{I_\sigma}^{\Delta\sigma} \left(\frac{r}{R}\right)^2, \tag{23}$$

where the last term on the right-hand side represents the solid angle (Modest 2003). At $R = 60$ km altitude, the solid angle of a 1 m radiative volume is 3×10^{-7} sr, and therefore the RTE integration ($\overline{I_\sigma}^{\Delta\sigma}$) is done on a single ray.

The magnitude [0 mag] of the different bands is written from Eq. 24 to 26. These equations compute the apparent and absolute magnitude. The difference between these two magnitudes is that the latter is computed by setting $R = 100$ km in Eq. 23. The constant after the integral is taken from Bessell (1990) and Bessell et al. (1998), which corresponds to the flux of Vega on the specific band.

$$M_V = -2.5\log\left(\sum_{\Delta\sigma} \overline{V_\sigma}^{\Delta\sigma} \cdot \overline{F_\sigma}^{\Delta\sigma} \Delta\sigma\right) - 13.72, \tag{24}$$

$$B = -2.5\log\left(\sum_{\Delta\sigma} \overline{B_\sigma}^{\Delta\sigma} \cdot \overline{F_\sigma}^{\Delta\sigma} \Delta\sigma\right) - 13.22, \tag{25}$$

$$R = -2.5\log\left(\sum_{\Delta\sigma} \overline{R_\sigma}^{\Delta\sigma} \cdot \overline{F_\sigma}^{\Delta\sigma} \Delta\sigma\right) - 13.76. \tag{26}$$

Ceplecha (1987) provides the following equation to transform the UBVRI into the panchromatic system and to compute the photographic magnitude M_p of meteor entry

$$M_p = M_V + 0.62(B - M_V) - 0.52(M_V - R). \tag{27}$$

The photography and visual intensity in 0 mag units is expressed as,

$$I^\star_\alpha = 10^{-0.4 M_\alpha}, \quad \alpha = p, V, \tag{28}$$

Verniani (1965), and the luminous efficiency with mag erg^{-1} s units,

$$\tau^\star_\alpha = \frac{I^\star_\alpha}{I_T} \tau_T, \quad \alpha = p, V, \tag{29}$$

where I_T is computed by Eq. 22 and τ_T by Eq. 21.

3. Results

Based on detailed simulations — for which flow, ablation, and radiation are coupled — it is possible to derive the coefficients used in the single body theory and to gain more in-depth knowledge on the meteor phenomenon, as opposed to analysis of observations alone. The physics behind this phenomenon is sensitive to numerous parameters, such as the size, trajectory, and composition of the bolide. In this section, we explore some of these parameters, and we derive absolute magnitude, heat-transfer, and luminous efficiency from detailed simulations. Moreover, we compute the spectra observed from ground spectrometers by solving the RTE on a line of sight from the stagnation point to the ground.

We divide the results section into two parts. In the first part, we present an application of the methodology to study iron and H5 chondrites of two different sizes (0.1 and 1 m radius) and at two different altitudes (60 and 50 km), with a velocity of 15 km s^{-1}. Within this study, we analyze the nonequilibrium effects in the flow due to radiation, and then we derive absolute magnitude, heat-transfer, and luminous efficiency. In the second part, we apply our methodology to study the entry of the Lost City bolide McCrosky et al. (1971), at 70, 60, 50, and 40 km, and compare the derived absolute magnitude with the observations.

3.1. Application of the methodology

3.1.1. Flow field analysis

The magnitude of the light curves is correlated with the size of the incoming object, which means that the radiation effects are stronger for larger objects. A strong radiative field induces nonequilibrium effects, especially in the free-stream where radiation can ionize and dissociate the flow. Moreover, at the typical regimes of meteor entry, the surface temperature highly depends on the incoming heat flux due to the radiative emission from the shock layer. Figures 3a and 3b show the temperature along the stagnation streamline for two H5 chondrites at 50 km altitude with different sizes (1.0 m on the left and 0.1 m on right). The surface temperature is approximately the same for both objects due to an energetic balance of incoming heat flux and mass removal, meaning that higher heat flux results in a higher evaporation rate (see Tab. 3). The vapor layer in front of the surface is characterized by a small increase in temperature (around 2000 K for the 1.0 m radius) followed by a shock layer in thermal equilibrium, where the translational and internal temperatures reach more than 14000 K. The shock is located at 80 mm and 7 mm for the 1 and 0.1 m bodies, respectively. Upstream from the shock, a substantial departure from thermal equilibrium is observed with an increase of the internal temperature. The excitation of the internal modes is due to the radiated energy from the shock layer, resulting in a decrease of temperature at the shock layer and boundary layer. The sudden equilibrium of T and T^{ve} upstream in Figures. 3a and 3b are artifacts of the boundary condition, but due to the large computation domain the shock layer results are unaffected. Moreover, at the free-stream, the energy transfer between the internal and translational mode (via VT energy transfer) leads to an increase of the translational temperature. The emission of photons leads to photochemistry reactions forming ionized and dissociated species at the free-stream (see Figs. 3c and 3d). From the radiative heat flux at the wall (Tab. 3) and the level of nonequilibrium in the free-stream, it is reasonable to conclude that the radiative emission is stronger for the 1 m object because of the size of the shock layer.

Under the conditions reported in this paper, the increase of the surface temperature induces intensive evaporation of the meteoroid, forming a vapor layer in front of the surface. Figures 3e and 3f show the vapor layer composed mostly by evaporation products, which extends to 35 mm for the larger and 2.4 mm for the smaller bolide. Moreover, the low dissociation energy of the alkali metals leads to evaporation in the form of atoms or diatomic molecules, as in the case of Na and SiO. As the temperature increases in the vapor layer (Fig. 3a), the SiO dissociates into Si and Na ionizes into Na$^+$. Although K is a volatile,

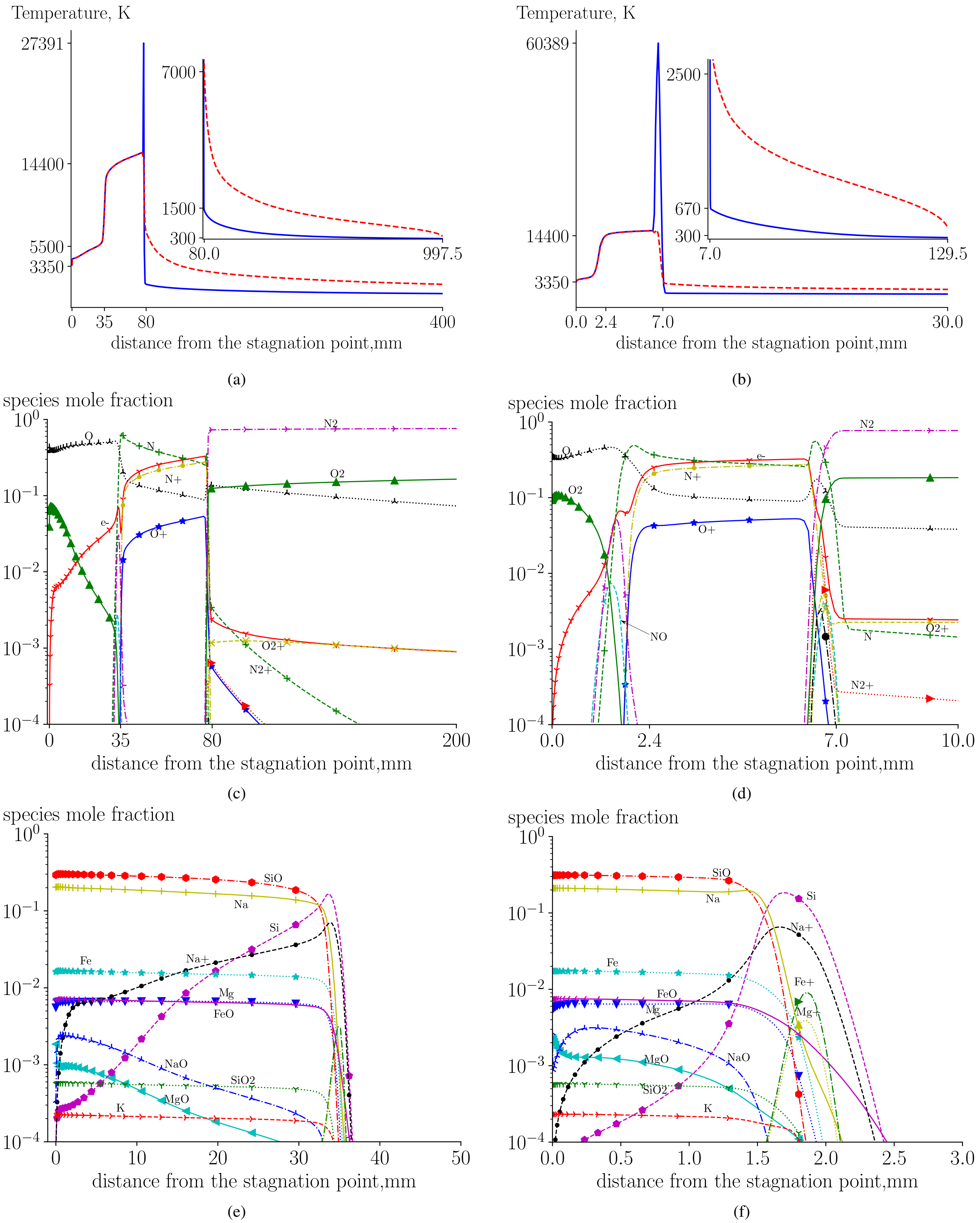

(a) (b) (c) (d) (e) (f)

Fig. 3: Flowfield results along the stagnation streamline of the H5 chondrite (a) temperature profile of the 1.0 m radius at 50 km altitude and (b) temperature profile of the 0.1 m radius at 50 km altitude: —— T, - - - T^{ve}; (c) composition of the air species of the 1.0 m radius at 50 km altitude; (d) composition of the air species of the 0.1 m radius at 50 km altitude; (e) composition of the evaporation products of the 1.0 m radius at 50 km altitude; (f) composition of the evaporation products of the 0.1 m radius at 50 km altitude.

its low composition in the condensed phase results in a residual presence in the gas phase. The refractory elements such as Ca, Al, and Ti have low vapor pressure, and therefore they are not present in the gas phase. The vapor layer is formed due to the strong blowing of evaporation gases pushing the air upstream. Furthermore, this vapor layer blocks the convective heat flux at the surface (in Tab. 3 the convective heat flux is a small contribution to the total heat flux). As reported by (Ceplecha et al. 1998), we identify the main spectrum as the radiative excitation of the atoms in the vapor layer (Figs 3e and 3f) and the secondary spectrum corresponds to the radiative excitation of the atoms in the shock layer (Figs. 3c and 3d). This identification consists of the temperature results where the main spectrum contains elements at a temperature of ≈ 3000 K, and the secondary spectrum contains elements of ≈ 14000 K as found by Borovička (1993, 1994).

Figure 4 shows the temperature profile (left figure) and the ablation composition (right figure) of a 1 m iron bolide at 50 km altitude with an entry velocity of 15 km s^{-1}. Figure 4b shows that the vapor layer near the surface is composed of pure iron which partially ionizes further upstream. Compared to Fig. 3a, Fig. 4a shows a similar temperature profile at the shock layer and the free-stream. This behavior suggests that the precursor effect is mainly sensitive to the entry conditions and the size of the object, and not to its composition. On the other hand, a thermal nonequilibrium is present in the vapor layer of the iron bolide (Fig. 4a) due to energy transfer from electron-impact ionization reactions. Even though the mole fraction of the electron in the vapor layer is similar for both the H5 and iron, the energy transfer due to ionization reactions is higher for the iron bolide. This study (see Tab. 4) reveals that the surface temperature is similar for bolides at the same altitude, and that the convective heat flux is negligible compared to the radiative heat flux, as for the H5 case. Also, in comparison with H5, the evaporation rate is higher for lower surface temperatures due to a higher equilibrium vapor pressure of pure iron for lower temperatures.

For the study presented here, the radiative heat flux is the major contribution to the total heat flux (see Tabs. 3 and 4). The convective heat flux has a small contribution to the total heat flux due to the high ablation rate, leading to a temperature plateau where the vapor layer is located, and therefore the gradients of composition and temperature are small. For the iron case, the radiative heat flux into the wall is more significant due to a smaller radiative absorption in the boundary layer. Figure 5 shows the radiative heat flux vector $q^{rad}(r)$ along the stagnation streamline. A negative value represents a radiative heat flux towards the surface, and a negative slope corresponds to the absorption of the participating medium. In contrast, a positive slope of the radiative heat flux corresponds to emission. Close to the surface, the H5 chondrite shows a steeper negative slope, meaning that the absorption in the boundary layer is larger than the iron case. The small deviation of the radiative heat flux above 60 mm is due to the difference in the stand-off shock-distance between the H5 chondrite and the iron case. Since the pure iron gas density at the surface is higher than the H5 chondrite, the blowing velocity for both cases is similar, and this is why the stand-off shock-distance is comparable for both cases.

3.1.2. Meteor coefficient from the flow field

The detailed flow field allows us to retrieve the heat-transfer coefficient, the luminous efficiency, and the observed absolute photographic magnitude. We recall that the latter is modeled by integrating the RTE over a line of sight from the stagnation point to the ground. It is necessary to consider the atmospheric conditions along the line of sight because the atmospheric O_2 Schumann-Runge (Nicolet & Peetermans 1980) absorbs part of the light. For the photographic magnitude in Eq. 27, we use the UBVRI filters from Bessell (1990) to compute the corresponding spectral intensity in the red, visible, and blue passband ranges. The difference between the photographic magnitude and the visual magnitude defines the color index CI, which quantifies the observed color of a meteor during entry.

Figure 6a shows the red, visible, and blue spectral intensity for the case presented in Fig. 3a. The results shown in Tab. 5 concern the magnitude in the different ranges for the entire H5 study from which a $CI > 0$ is estimated, contradicting the observations of this type of bolide (Ceplecha & ReVelle (2005); ReVelle & Rajan (1979); Jacchia & Whipple (1961)). The strong red and visible passband emission are due to the spectral intensity of Na (see Fig. 6c) resulting from its composition in the vapor layer. Borovička & Betlem (1997) attributes a $CI < 0$ to the emission of CaII lines in the blue passband. The models presented in this paper are unable to predict the presence of Ca because the vapor pressure computed from Magma is $O(4)$ lower than the volatile at these conditions (Na), and therefore the evaporation of this element is negligible. In conclusion, $CI > 0$ because of the absence of Ca and the low content of Fe and Mg combined with the strong presence of Na.

Figure 6c shows the spectral intensity of each evaporated atom while Fig. 6b shows the air species. In the visible range (between 12500 and 25000 cm^{-1}) the spectrum is dominated by O, N, and Na, while Si, Fe, and Na^+ are more intense in the UV region. In the near-infrared, the spectrum is mainly dominated by Na, N, and O and above 70000 cm^{-1}, only O, N, O^+ and N^+ are found.

Figure 7a shows the spectral intensity through the different filters for the iron bolide case presented in Fig. 4. In this case, the blue passband is more intense than the H5 chondrite (see Tab. 6) because of the spectral intensity of Fe in Fig. 7c. We recall that the vapor layer is mostly composed of pure Fe with a small trace of Fe^+. The emission of Fe^+ is outside the range observed by the photographic cameras. As a consequence of the strong Fe emission, the CI turns negative for all the cases performed on the iron bolide, as shown in Tab. 6.

The total intensity in Eq. 22 is obtained by integrating the total spectral intensity shown in figures 6a and 7a. We highlight the fact that term r in Eq. 22 corresponds to a distance from which the radiative power is zero, which is approximately double the sphere radius. From the visual and photography magnitude (Tabs. 5 and 6), one can estimate the corresponding intensity from Eq. 28 and the luminous efficiency from Eq. 29. Table 7 shows the different luminous efficiency (a negative CI corresponds to a $\log \tau_p - \log \tau_v > 0$ and vice-versa) and the heat-transfer coefficient (Eq. 20) for all cases presented here. Our results allow us to conclude that the luminous efficiency does not depend only on the velocity, as is typically assumed, but on the size, composition, and altitude. Although our definition of C_h is different from that of Johnston et al. (2018), we estimate similar values for the H5 chondrite. Table 7 also shows that the heat-transfer coefficient for iron is higher than that for H5 chondrite due to a higher total heat flux entering the iron surface (Tab. 4) compared to that entering H5 (Tab. 3).

3.2. Lost City bolide

The Lost City bolide (McCrosky et al. 1971) has the advantage of having a low entry velocity and fragmentation occurring be-

Table 3: Parameters concerning the SEB and SMB on the H5 chondrite

Alt. [km]	Rad. [m]	T_{w} [K]	$\dot{m}_{\mathrm{vap}}$ [kg s^{-1} m^{-2}]	$\epsilon q_{rad,in}$ [MW m^{-2}]	q_{conv} [MW m^{-2}]	$\epsilon\sigma T_w^4$ [MW m^{-2}]	$\dot{m}_{\mathrm{vap}}\mathrm{L}_{\mathrm{heat}}$ [MW m^{-2}]
50	0.1	3352.9	5.3	34.56	3.35	6.09	31.82
50	1.0	3354.6	8.7	56.19	1.92	6.1	52.01
60	0.1	3103.9	0.8	8.52	0.95	4.48	5.0
60	1.0	3110.1	2.3	17.36	0.78	4.51	13.64

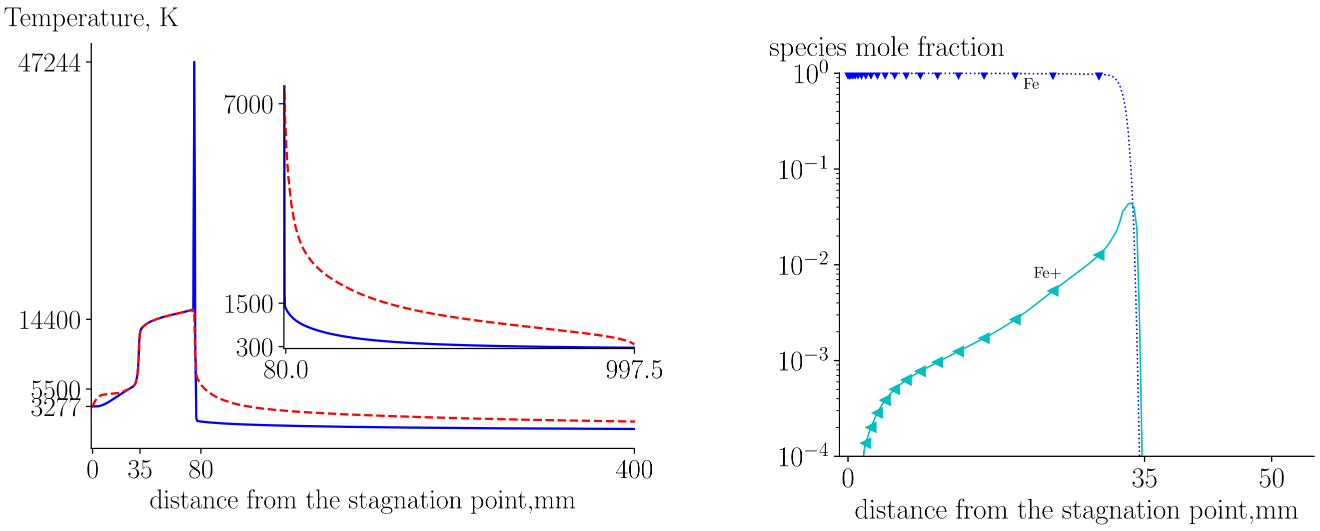

(a)

(b)

Fig. 4: Flowfield results along the stagnation streamline of the iron meteoroid (a) temperature profile of the 1.0 m radius at 50 km altitude: —— T, - - - T^{ve}; (b) composition of the evaporation products of the 1.0 m radius at 50 km altitude.

Table 4: Parameters concerning the SEB and SMB from the iron meteoroid

Alt. [km]	Rad. [m]	T_{w} [K]	$\dot{m}_{\mathrm{vap}}$ [kg s^{-1} m^{-2}]	$\epsilon q_{rad,in}$ [MW m^{-2}]	q_{conv} [MW m^{-2}]	$\epsilon\sigma T_w^4$ [MW m^{-2}]	$\dot{m}_{\mathrm{vap}}\mathrm{L}_{\mathrm{heat}}$ [MW m^{-2}]
50	0.1	3265.3	6.0	40.9	0.11	5.48	36.77
50	1.0	3276.8	12.0	78.8	0.01	5.58	73.2
60	0.1	2985.8	1.1	9.63	0.78	3.83	6.41
60	1.0	3006.2	2.9	20.85	0.01	3.94	17.45

Table 5: Total intensity and absolute light magnitude obtained from the H5 chondrite

Alt. [km]	Rad. [m]	$I_{\mathrm{T}}/10^{14}$ [erg s^{-1}]	M_V [mag]	(B-M_V) [mag]	(M_V-R) [mag]	M_p [mag]
50	0.1	3.88	-8.45	1.27	0.71	-8.03
50	1.0	90.1	-14.59	0.98	0.70	-14.24
60	0.1	1.22	-7.36	1.54	0.84	-6.85
60	1.0	21.0	-12.65	1.00	0.95	-12.52

Table 6: Total intensity and absolute light magnitude obtained from the iron meteoroid

Alt. [km]	Rad. [m]	$I_{\mathrm{T}}/10^{14}$ [erg s^{-1}]	M_V [mag]	(B-M_V) [mag]	(M_V-R) [mag]	M_p [mag]
50	0.1	4.35	-8.44	-0.75	-0.20	-8.80
50	1.0	92.6	-14.09	-0.29	0.09	-14.32
60	0.1	1.37	-7.14	-0.77	-0.11	-7.56
60	1.0	22.3	-12.30	-0.43	0.06	-12.59

Table 7: Luminous efficiency and heat-transfer coefficient obtained from the H5 chondrite and the iron meteoroid

Type	Alt. [km]	Rad. [m]	$\log\tau_v^\star$ [mag erg^{-1} s]	$\log\tau_p^\star$ [mag erg^{-1} s]	$C_h/10^{-2}$
H5	50	0.1	-11.42	-11.59	2.3
	50	1.0	-11.25	-11.35	3.52
	60	0.1	-11.08	-11.28	1.95
	60	1.0	-11.40	-11.45	3.73
Iron	50	0.1	-11.54	-11.39	2.56
	50	1.0	-11.59	-11.50	4.78
	60	0.1	-11.33	-11.16	2.09
	60	1.0	-11.67	-11.55	4.39

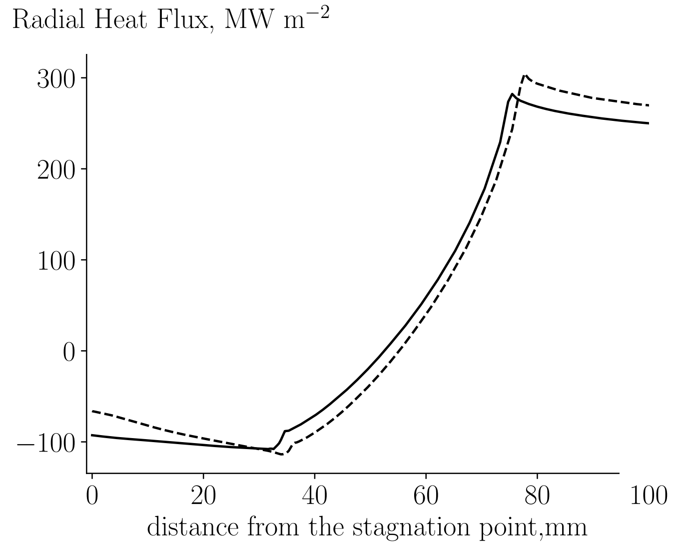

Fig. 5: Radiative heat flux along the stagnation streamline 1.0 m radius at 50 km: The solid line represents iron, and the dashed line represents H5 chondrite.

low 40 km. Thus, it is adequate to evaluate our model, which does not include fragmentation. The size and the trajectory conditions are well documented in Ceplecha & ReVelle (2005), and we use those as boundary conditions in our simulation tools. We simulate the flow field of the bolide at four trajectory points (70, 60, 50 and 40 km) from which the radius of roughly 0.23 m and the velocity of 14.15 km s^{-1} are almost constant according to the results of Ceplecha & ReVelle (2005). Moreover, we consider that the Lost City bolide is an H5 chondrite (Borovička et al. (2015)) with the same composition as the previous test case. The same methodology as in the previous section is used to compute the radiative intensity and the absolute magnitude from the flow field.

Figure 8 shows the comparison of the observed absolute magnitude with the numerical results; here the observation error is less than 0.5 mag (McCrosky et al. (1971); Ceplecha & ReVelle (2005)). The absolute magnitude M_p shows a small deviation from the observation. This deviation motivates a different approach to treat the evaporation boundary conditions, which disregard the evaporation of volatiles. In other words, the total vapor pressure is obtained from Magma, and the species vapor pressure is computed via Dalton's laws, forcing the composition of the alkali metals at the surface to be the same as in Tab. 2. This enforcement of the composition follows a more qualitative rather than a quantitative treatment of the boundary condition since it disregards the evaporation of volatiles. Nonetheless, when we estimate the absolute magnitude ($M_{p,equil}$) using this modified boundary condition, we obtain better agreement with the observations. The standard and modified boundary conditions predict the evaporation of different species from the material which affects the flow field around the bolide. Figure 9 shows the flow field of Lost City bolide at 50 km; the left and right columns correspond to the simulation with the standard and the modified boundary conditions, respectively. The two top figures show the temperature along the stagnation line, where no significant differences are observed, and the two bottom figures show the composition of the evaporated species. In the left figure (standard boundary condition), the two major species in the flow are SiO and Na, followed by the presence of small amount of Fe

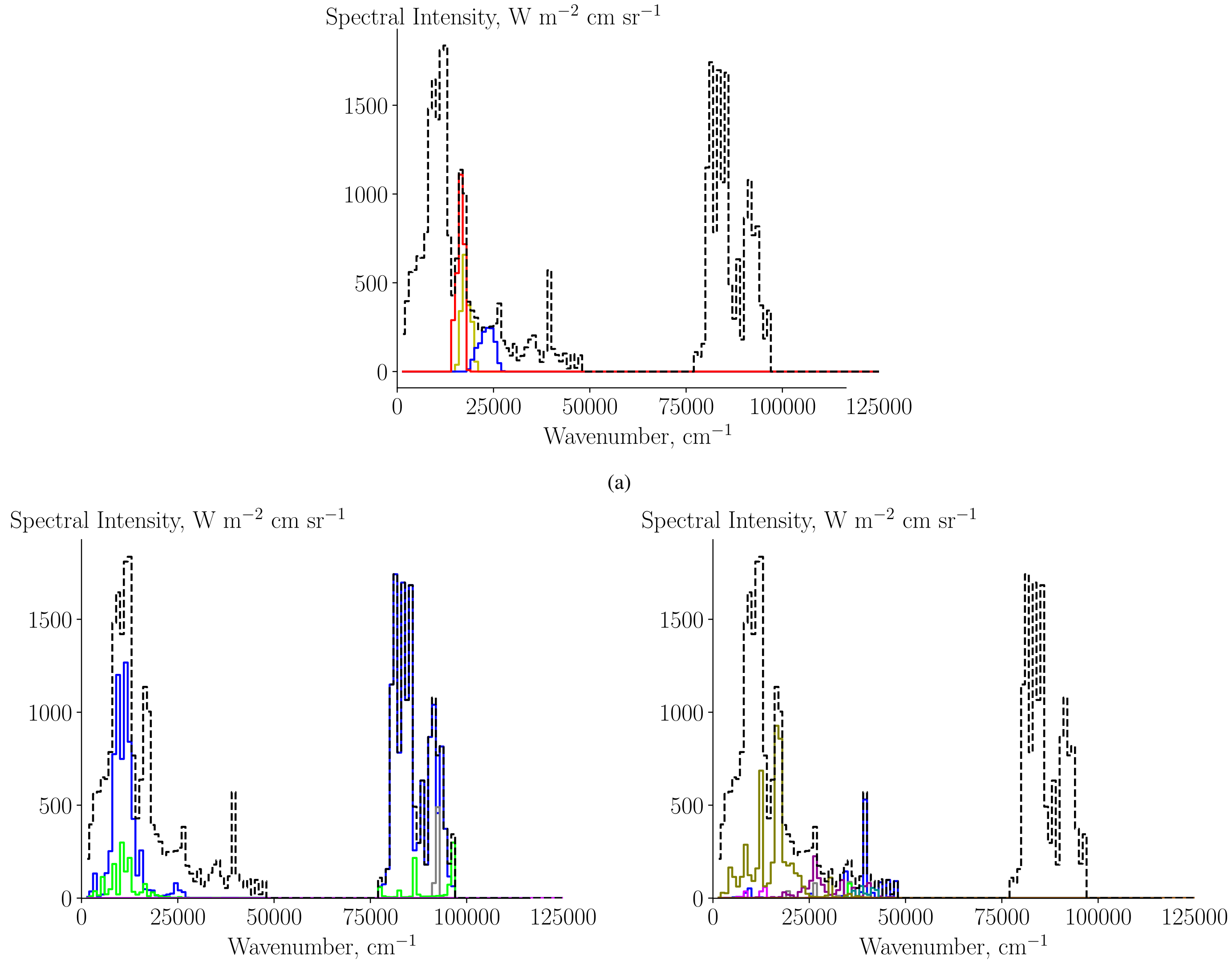

(a)

(b)

(c)

Fig. 6: Narrowband spectral intensity of the 1.0 m radius of the H5 chondrite at 50 km altitude (a) comparison between the total spectral intensity (- - -) with the blue (——), visible (——) and red (——) passband; (b) spectral intensity of the air atomic lines: —— N, —— N$^+$, —— O, —— O$^+$, - - - total; (c) spectral intensity of the atomic lines concerning the most abundant evaporation products: —— Si, —— Mg, —— Mg$^+$, —— K, —— Fe, —— Fe$^+$, —— Na, —— Na$^+$, - - - total.

and Mg. Molecules of SiO and Na dissociate and ionize further downstream creating Si and Na$^+$. The volatile nature of Na leads to a substantial amount of this species being present in the flow, differently from the species formed by Ca. In the right figure, the modified boundary condition estimates SiO$_2$, MgO, and FeO as the major species. This figure also shows traces of Ca, which were not present in the previous example, and the composition of Na decreases significantly.

The difference of the absolute magnitude in Fig. 8 is a consequence of the species generated by both boundary conditions. The modification of the boundary condition impacts the flow field around the Lost City bolide and its spectra calculation. In the standard boundary condition case, the abundant presence of Na (Fig. 10c) leads to a strong spectral intensity in the red and visible range (Fig. 10a), meaning that the color index is positive. Moreover, the presence of a relatively small amount of Fe and Mg leads to a weak intensity in the blue region. The weak intensity of the blue region is also explained by the lack of Ca and Ca$^+$, which are strong radiators in this range Borovička & Betlem (1997). On the other hand, when the modified boundary condition is used, the color index becomes negative which is due to a stronger emission in the blue region (Fig. 10b) caused by the presence of Mg, Fe, Ca, and Ca$^+$. Figure 10d shows a strong emission of these atoms from 200000 to 300000 cm^{-1}. In this case, the presence of Ca and Ca$^+$ is clearly identified, confirming several spectroscopy observations from meteor observation Borovička (1993, 1994); Borovička & Betlem (1997). Finally, the discrepancy between the observations and the numerical simulations might be attributable to the fact that we are not considering the wake. The work of Johnston & Stern (2019) shows that the wake contributes significantly to the radiative flux observed from the ground for Tunguska-type bolides.

These results appear counterintuitive because, on one hand, we present a physical boundary condition (standard boundary condition) that overestimates the composition of Na and cannot predict the appearance of Ca, and on the other hand, we have a

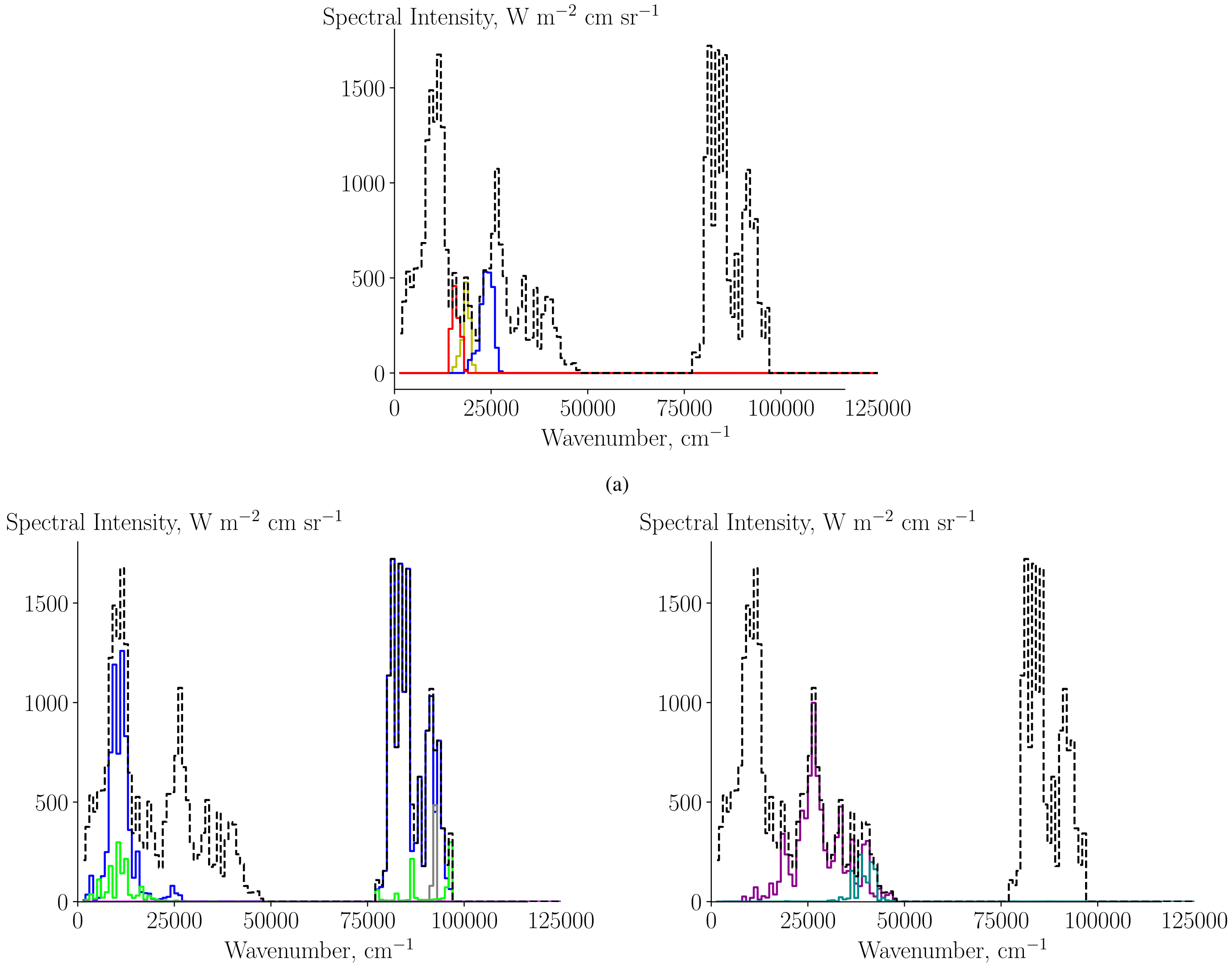

(a)

(b)

(c)

Fig. 7: Narrowband spectral intensity of the 1.0 m radius of the iron meteoroid at 50 km altitude (a) comparison between the total spectral intensity (- - -) with the blue (——), visible (——) and red (——) passband; (b) spectral intensity of the air atomic lines: —— N, —— N$^+$, —— O, —— O$^+$, - - - total; (c) spectral intensity of the evaporation atomic lines: —— Fe, —— Fe$^+$, - - - total.

boundary condition (modified boundary condition) which does not distinguish the evaporation of volatile and refractory elements but provides a better qualitative agreement with the spectroscopic measurements. This contradiction could be explained by considering that the molten surface breaks up into small droplets which completely evaporate in the trail. The break up of the molten layer into small droplets was explored by Capek et al. (2019), where the author was able to replicate the light curves of iron meteoroids by fitting the luminous efficiency. Nonetheless, spraying of the molten layer seams to be the most plausible explanation for the appearance of refractory elements in the spectra, as was also the conclusion of Borovička (1993). The rationale proposed here can also be supported by the experimental spectra of (Drouard et al. 2018), which does not consider the spraying of the molten thickness. From the high-resolution spectra, these latter authors observed an overestimation of Na with respect to Fe and Mg and a weak intensity of refractory Ca.

4. Conclusion

Inspired by the design of thermal protection systems applied to hypersonic re-entry vehicles, this paper presents a methodology that we develop to study meteor entry. We focus on the plasma flow around the bolide, and we assume a nonfragmenting body with a perfect spherical shape. Within these assumptions, we derive luminous efficiency and heat-transfer coefficients used in heuristic models by meteor astronomers. This methodology also allows one to simulate the corresponding spectrum observed by the ground spectrometers thanks to a detailed description of the flow field, which cannot be exploited by the single-body theory.

We applied the methodology to different bolide compositions, altitudes, and sizes, while the velocity was kept constant. We observe that the luminous efficiency depend on all of these parameters, and not only on the velocity as the classical theory typically assumes. The bolide size and altitude determine the shock layer radiative intensity and, consequently, the intensity of the luminosity. Moreover, we observe that the radiative inten-

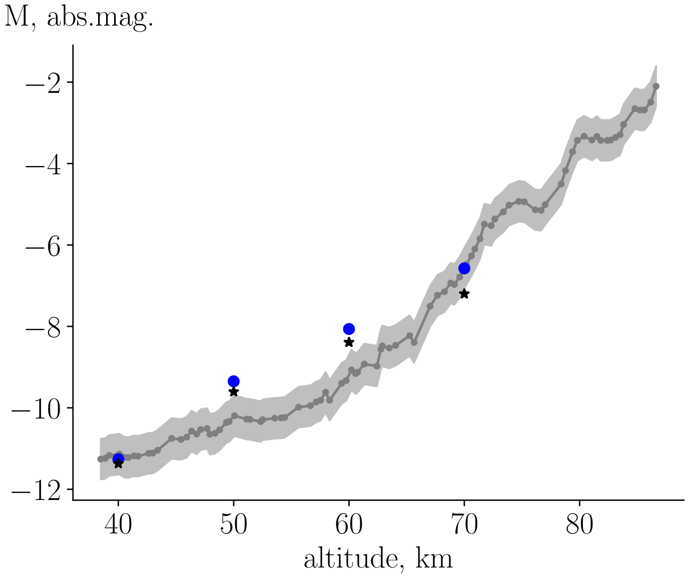

Fig. 8: Absolute magnitude luminosity of the Lost City bolide; comparison between the observations and the numerical results using standard and modified boundary conditions: (gray area) observations with uncertainty, ● absolute light magnitude based on the standart boundary condition (M_p), ★ absolute light magnitude based on the modified boundary condition ($M_{p,equil}$)

sity of the air mechanisms on the shock layer is relevant for the estimation of the luminous efficiency.

We apply our models to the entry of the Lost city bolide. This bolide is suitable because it suffered fragmentation below 40 km, meaning that we could test our models above this altitude up to the continuum limit. Our results show a more prominent color index than the one inferred from observations for this type of bolide. We believe that this discrepancy in the color index is due to the evaporation of droplets arising from the molten material. A multidimensional computational fluid dynamics (CFD) solver would be needed to study the effect of droplet evaporation on the wake, which is out of the scope of this paper. Nevertheless, this methodology can be applied to deduce the composition and the size of the bolide at a reasonable computational cost.

Acknowledgements. The authors are thankful to Dr. Anouar Soufiani, Dr. Philippe Rivière and Dr. Laurent Socausse (Laboratoire EM2C, CentraleSupélec, Université Paris-Saclay) for the valuable insight on the radiative properties. We are also thankful to the reviewer for the helpful comments. The research of B. D. is funded by a PhD grant of the Funds for Research Training in Industry and Agriculture (FRIA).

References

Akhmadov, U., Zaslonko, I., & Smirnov, V. 1988, Kinet. Catal. (Engl. Transl.); (United States), 29:2
Alexander, C. M. O. 2001, Meteoritics & Planetary Science, 36, 255
Baldwin, B. & Sheaffer, Y. 1971, Journal of Geophysical Research, 76, 4653
Bariselli, F., Frezzotti, A., Hubin, A., & Magin, T. E. 2019, Monthly Notices of the Royal Astronomical Society, 492, 2308
Bessell, M. S. 1990, Publications of the Astronomical Society of the Pacific, 102, 1181
Bessell, M. S., Castelli, F., & Plez, B. 1998, Astronomy & Astrophysics, 333, 231
Borovička, J. 1994, Astronomy & Astrophysics, 103, 83
Borovička, J. & Berezhnoy, A. 2016, Icarus, 278, 248
Borovička, J. & Betlem, H. 1997, Planetary and Space Science, 45, 563 , Asteroids, Comets, Meteors 1996
Borovička, J., Spurný, P., & Brown, P. 2015, Asteroids IV
Borovička, J., Stork, R., & Bocek, J. 1999, Meteoritics & Planetary Science, 34, 987
Borovička, J. 1993, Astronomy & Astrophysics, 279, 627
Boyd, I. 2000, Earth, Moon and Planets, 82-83, 93
Bronshten, V. A. 1983, Physics of Meteoric Phenomena (D. Reidel Pub. Co.)
Capek, D., Koten, P., Borovička, J., et al. 2019, Astronomy & Astrophysics, 625, A106
Ceplecha, Z. 1987, Bulletin of the Astronomical Institutes of Czechoslovakia, 38, 222
Ceplecha, Z. 1996, Astronomy & Astrophysics, 311, 329
Ceplecha, Z., Borovička, J., Elford, W. G., et al. 1998, Space Science Reviews, 84, 327
Ceplecha, Z., Borovička, J., & Spurný, P. 2000, Astronomy & Astrophysics, 357, 1115
Ceplecha, Z. & ReVelle, D. O. 2005, Meteoritics & Planetary Science, 40, 35
Cunto, W., Mendoza, C., Ochsenbein, F., & Zeippen, C. J. 1993, Astronomy & Astrophysics, 275
Drouard, A., Vernazza, P., Loehle, S., et al. 2018, Astronomy & Astrophysics, 613, A54
Fegley, B. & Cameron, A. 1987, Earth and Planetary Science Letters, 82, 207
Gnoffo, P., Gupta, R., & Shinn, J. 1989, Conservation equations and physical models for hypersonic air flows in thermal and chemical nonequilibrium, Technical Paper 2867, NASA
Golub, A. P., Kosarev, I. B., Nemchinov, I. V., & Shuvalov, V. V. 1996, Solar System Research, 30, 183
Gritsevich, M. & Koschny, D. 2011, Icarus, 212, 877
Hartung, L. C., Mitcheltree, R. A., & Gnoffo, P. A. 1992, Journal of Thermophysics and Heat Transfer, 6, 412
Hodgson, A. & Mackie, J. 1979, Combustion and Flame, 35, 323
Howie, R. M., Paxman, J., Bland, P. A., et al. 2017, Experimental Astronomy, 43, 237
Jacchia, L. G. & Whipple, F. L. 1961, Smithsonian Contributions to Astrophysics, 4, 97
Jarosewich, E. 1990, Meteoritics, 25, 323
Jenniskens, P. 2004, Advances in Space Research, 33, 1444 , the Impact of Minor Bodies of Our Solar System on Planets and Their Middle and Upper Atmosphere
Jenniskens, P., Wilson, M. A., Packan, D., et al. 1998, Earth, Moon, and Planets, 82, 57
Johnston, C. & Stern, E. 2017, in 47th AIAA Thermophysics Conference, (Denver, Colorado), AIAA 2017-4533
Johnston, C. O. & Stern, E. C. 2019, Icarus, 327, 48
Johnston, C. O., Stern, E. C., & Wheeler, L. F. 2018, Icarus, 309, 25
Kashireninov, O., Kuznetsov, V., & Manelis, G. 1977, AIAA Journal, 15, 1035
Kitamura, K. & Shima, E. 2013, Journal of Computational Physics, 245, 62
Klomfass, A. & Muller, S. 2000, A Quasi-One Dimensional Approach for Hypersonic Stagnation-Point Flows, Tech. rep., RWTH Aachen
Kramida, A. & Ralchenko, Y. 1999, NIST Atomic Spectra Database, NIST Standard Reference Database 78
Lamet, J., Rivière, P., Perrin, M., & Soufiani, A. 2010, Journal of Quantitative Spectroscopy and Radiative Transfer, 111, 87
Lamy, H., Ranvier, S., Keyser, J., Gamby, E., & Calders, S. 2011, Meteoroids Conference Proceedings, NASA/CP–2011–216469, 351
Lasaga, A. C. & Cygan, R. T. 1982, American Mineralogist, 67, 328
Laux, C. 2002, in Physico-Chemical Modeling of High Enthalpy and Plasma Flows, ed. Fletcher, D., Charbonnier, J.M., Sarma, G.S.R., and Magin, T., VKI LS 2002-07, von Karman Institute for Fluid Dynamics, Rhode-Saint-Genèse, Belgium
Le Picard, S. D., Canosa, A., Reignier, D., & Stoecklin, T. 2002, Phys. Chem. Chem. Phys., 4, 3659
Lide, D. R., ed. 2004, CRC Handbook of Chemistry and Physics, 84th edn. (CRC Press LLC Boca Raton.)
Lopez, B., Perrin, M., Rivière, Ph., & Soufiani, A. 2013, Journal of Thermophysics and Heat Transfer, 27, 404
Madiedo, J. M., Trigo-Rodríguez, J. M., Konovalova, N., et al. 2013a, Astronomy & Astrophysics, 555, A149
Madiedo, J. M., Trigo-Rodríguez, J. M., Ortiz, J. L., et al. 2013b, Monthly Notices of the Royal Astronomical Society, 435, 2023
Magin, T. E. 2004, PhD thesis, Universitè Libre de Bruxelles
Magin, T. E., Panesi, M., Bourdon, A., Jaffe, R. L., & Schwenke, D. W. 2012, Chemical Physics, 398, 90 , chemical Physics of Low-Temperature Plasmas (in honour of Prof Mario Capitelli)
McBride, B. J., Gordon, S., & Reno, M. A. February 2001, Thermodynamic Data for Fifty Reference Elements, NASA TP-3287-REV1, Glenn Research Center, Cleveland, Ohio
McCrosky, R. E. & Ceplecha, Z. 1970, Bulletin of the Astronomical Institutes of Czechoslovakia, 21, 271
McCrosky, R. E., Posen, A., Schwartz, G., & Shao, C.-Y. 1971, Journal of Geophysical Research (1896-1977), 76, 4090

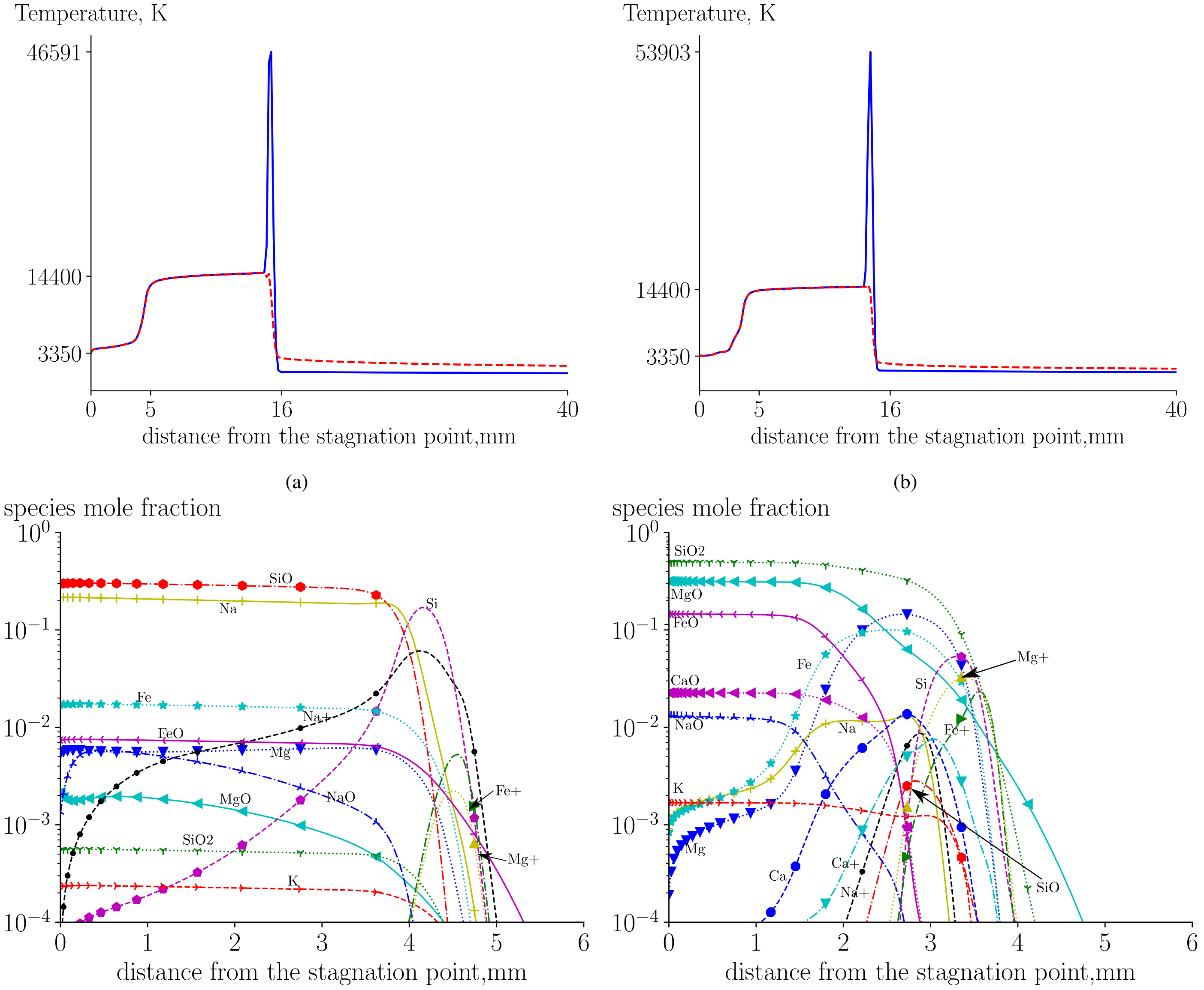

(a)

(b)

(c)

(d)

Fig. 9: Flowfield results along the stagnation streamline of the Lost City; comparison of the standard and modified boundary conditions (a) temperature profile at 50 km altitude with the standard boundary condition and (b) temperature profile at 50 km altitude with the modified boundary condition: —— T, - - - T^{ve}; (c) composition of the evaporation products at 50 km altitude with the standard boundary condition; (d) composition of the evaporation products at 50 km altitude with the modified boundary condition.

McGee, B. C., Hobbs, M. L., & Baer, M. R. 1998, Exponential 6 Parameterization for the JCZ3-EOS, SAND98-1191, Sandia National Laboratories
Mick, H.-J., Burmeister, M., & Roth, P. 1993, AIAA Journal, 31, 671
Millikan, R. C. & White, D. R. 1963, The Journal of Chemical Physics, 39, 3209
Modest, M. F. 2003, Radiative Heat Transfer, 2nd edn. (Academic Press)
Munafò, A. & Magin, T. E. 2014, Physics of Fluids, 26, 097102
Nicolet, M. & Peetermans, W. 1980, Planetary and Space Science, 28, 85
Park, C. 1988, Journal of Thermophysics and Heat Transfer, 2, 8
Park, C. 1989, Journal of Thermophysics and Heat Transfer, 3, 233
Park, C. 1993, Journal of Thermophysics and Heat Transfer, 7, 385
Park, C. 2013, Journal of Quantitative Spectroscopy and Radiative Transfer, 127, 158
Park, C. 2014, Journal of Thermophysics and Heat Transfer, 28, 598
Park, C. 2015, Journal of Quantitative Spectroscopy and Radiative Transfer, 154, 44
Park, C., Jaffe, R., & Partridge, H. 2001, Journal of Thermophysics and Heat Transfer, 15, 76
Plane, J. M. C. & Husian, D. 1986, J. Chem. Soc., Faraday Trans. 2, 82, 2047
ReVelle, D. O. & Rajan, R. S. 1979, Journal of Geophysical Research: Solid Earth, 84, 6255
Scoggins, J. B., Leroy, V., Bellas-Chatzigeorgis, G., Dias, B., & Magin, T. E. 2020, arXiv:2002.01783v1 [physics.comp-ph] [`arXiv:2002.01783`]
Scoggins, J. B. & Magin, T. E. 2015, Combustion and Flame, 162, 4514
Shuvalov, V. & Artemieva, N. 2002, Planetary and Space Science, 50, 181
Silber, E. A., Hocking, W. K., Niculescu, M. L., Gritsevich, M., & Silber, R. E. 2017, Monthly Notices of the Royal Astronomical Society, 469, 1869
Smith, G. P., Golden, D. M., Frenklach, M., et al. 1999, GRI-Mech 3.0. `http://www.me.berkeley.edu/gri_mech/`
Soucasse, L., Scoggins, J., Riviere, P., Magin, T., & Soufiani, A. 2016, Journal of Quantitative Spectroscopy and Radiative Transfer, 180, 55
Subasinghe, D. & Campbell-Brown, M. 2018, The Astronomical Journal, 155, 88
Svehla, R. A. 1962, Estimated Viscosities and Thermal Conductivities of Gases at High Temperatures, NASA TR R-132, Lewis Research Center, Cleveland, Ohio
Svettsov, V. V., Shuvalov, V. V., & Popova, O. P. 2018, Solar System Research, 52, 195

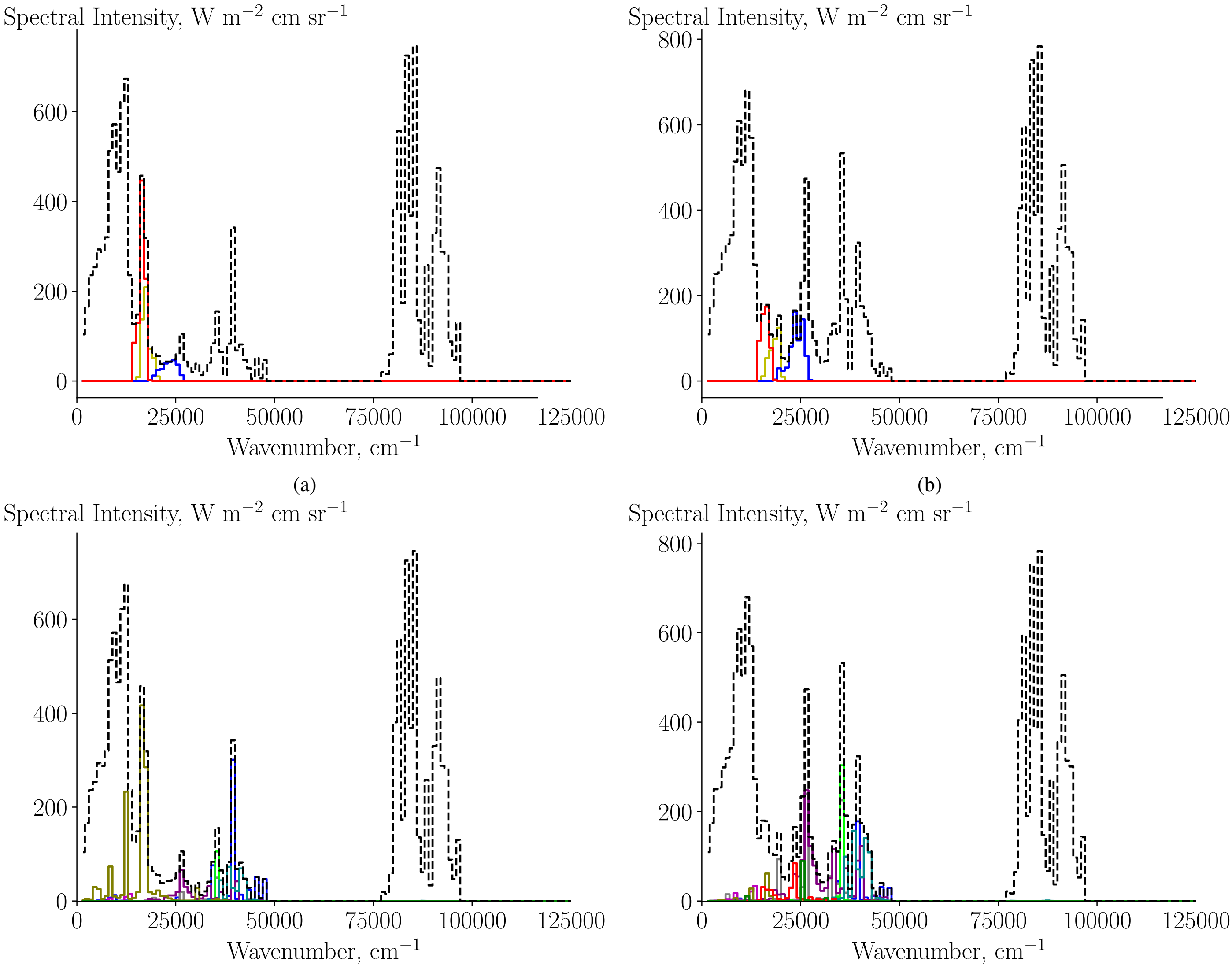

(a)

(b)

(c)

(d)

Fig. 10: Narrowband spectral intensity of the Lost City at 50 km altitude; comparison of the standard and modified boundary conditions (a) spectral intensity with standard boundary condition and (b) modified boundary condition: total (- - -), blue (——), visible (——), and red (——) passbands; (c) spectral intensity of the atomic lines concerning the most abundant evaporation products computed from the standard boundary condition and (d) spectral intensity of the atomic lines concerning the most abundant evaporation products computed from the modified boundary condition: —— Si, —— Mg, —— Mg$^+$, —— K, —— Fe, —— Fe$^+$, —— Na, —— Na$^+$, —— Ca, —— Ca$^+$, - - - total.

Verniani, F. 1965, Smithsonian Contributions to Astrophysics., 8, 141–171
Vojáček, V., Borovička, J., Koten, P., Spurný, P., & Štork, R. 2015, Astronomy & Astrophysics, 580, A67
Vondrak, T., Plane, J. M., Broadley, S., & Janches, D. 2008, Atmospheric Chemistry and Physics, 8, 7015
Weryk, R., Campbell-Brown, M., Wiegert, P., et al. 2013, Icarus, 225, 614
Wright, M. J., Hwang, H. H., & Schwenke, D. W. 2007, AIAA Journal, 45, 281
Öpik, E. J. 1958, Physics of meteor flight in the atmosphere.

Appendix A: Filter

The luminosity equations:

$$I_\alpha = 4\pi r^2 \int_0^\infty \alpha_\sigma \cdot I_\sigma d\sigma, \quad \alpha = T, V, B, R, \tag{A.1}$$

from which α_σ corresponds to the specific passband filter.

The term inside the integral of Eq. A.3 can be written as a narrow-band average following the definition:

$$\overline{X}^{\Delta\sigma} \equiv \frac{1}{\Delta\sigma}\int\limits_{\sigma_1}^{\sigma_2} X\Delta\sigma, \tag{A.2}$$

such that Eq. A.3 becomes

$$I_\alpha = 4\pi r^2 \sum_{\Delta\sigma} \overline{\alpha_\sigma I_\sigma}^{\Delta\sigma}\Delta\sigma, \quad \alpha = T, V, B, R. \tag{A.3}$$

In order to use the RTE solution from the SNB method, the following expression has to be verified:

$$\overline{\alpha_\sigma I_\sigma}^{\Delta\sigma} \approx \overline{\alpha_\sigma}^{\Delta\sigma} \cdot \overline{I_\sigma}^{\Delta\sigma} \tag{A.4}$$

and this separation is possible if the filter function α_σ is uncorrelated from the spectral intensity I_σ. To this end, we use the Specair library Laux (2002) to generate and a high-resolution spectrum with which to test the expression A.4. Figure A.1a shows the visible passband filter (taken from Bessell (1990)) averaged over a narrow band while Fig. A.1b shows the high-resolution spectral intensity and the corresponding narrow-band spectral intensity. Finally, Fig. A.1c shows both sides of the expression A.4.

The relative error between the two curves is approximately 1.5%, which leads us to conclude that the expression A.4 conserves the luminosity equation. This verification is also applicable to the Eq. 24 to 26.

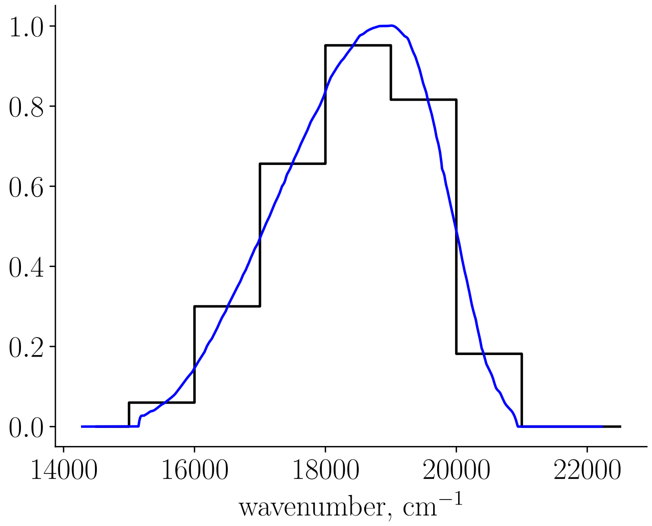

(a)

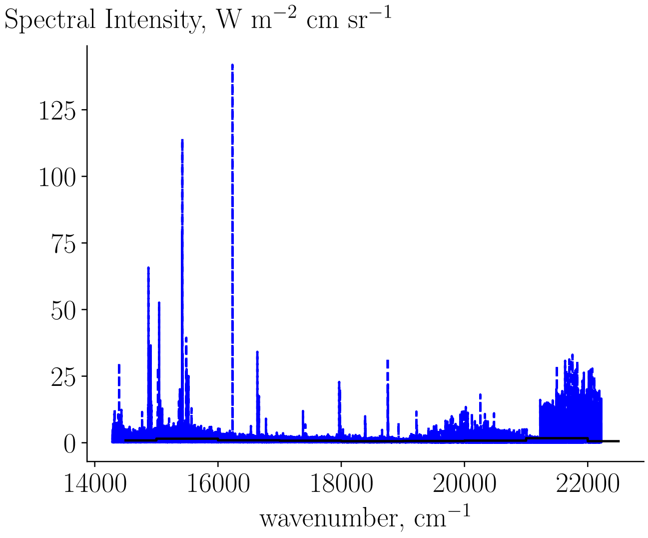

(b)

Appendix B: Physicochemical properties

Appendix B.1: Thermodynamic properties

For atoms, the separation between translational and electronic modes is valid since they are independent. Thermodynamic properties such as specific heat, enthalpy, and entropy are computed based on the system partition function (Eq. B.1). Typically, metallic species are characterized by having a low ionization energy and hundreds of energy levels, making the evaluation of the partition function computationally expensive due to its exponential nature.

To circumvent this problem, we use a binning strategy (Magin et al. 2012) which consists in grouping the energy levels into bins over an energy grid $[\varepsilon_k, \varepsilon_{k+1}[$, (Fig. B.1) as follows:

$$F_k = \{i \in F_e \text{ such that } (\varepsilon_k \leq E_i < \varepsilon_{k+1})\}, \quad k \in K_e,$$

where K_e is the set of the indices for the bins. An average energy for bin k follows:

$$\overline{E}_k = \frac{\sum_{i\in F_k} g_i E_i}{\overline{g}_K}, \quad k \in K_e,$$

based on the degeneracy of the bin as $\overline{g}_k = \sum_{i\in F_k} g_i$. Finally the electronic partition function assuming a reduced number of energy levels estimated for each bin is computed using Eq. B.1:

$$\overline{Q}_i^E(T = T^{ve}) = \sum_{k\in K_e} \overline{g}_k \exp\left(\frac{-\overline{\theta}_k}{T}\right), \quad i \in N_s, \tag{B.1}$$

where the characteristic temperature $\overline{\theta_k} = \overline{E}_k / k_b$ and k_b is the Boltzmann constant. As mentioned above, once the electronic partition function is known, computation of the thermodynamic properties becomes trivial. The electronic enthalpy follows:

$$h_i^E(T = T^{ve}) = R_i T^2 \frac{\partial \ln \overline{Q}_i^E}{\partial T}, \quad i \in N_s, \tag{B.2}$$

where R_i is the specific gas constant for species i. The total enthalpy of the atom:

$$h = \sum_{i\in N_s} y_i (h_i^T + h_i^E), \tag{B.3}$$

where the translational contribution is defined as $h_i^T(T) = 5/2 R_i T$.

The electronic levels for atoms are either observed through spectroscopy measurements or computed from quantum mechanics. The Nist database (Kramida & Ralchenko 1999) comprises a large amount of data regarding the electronic levels for

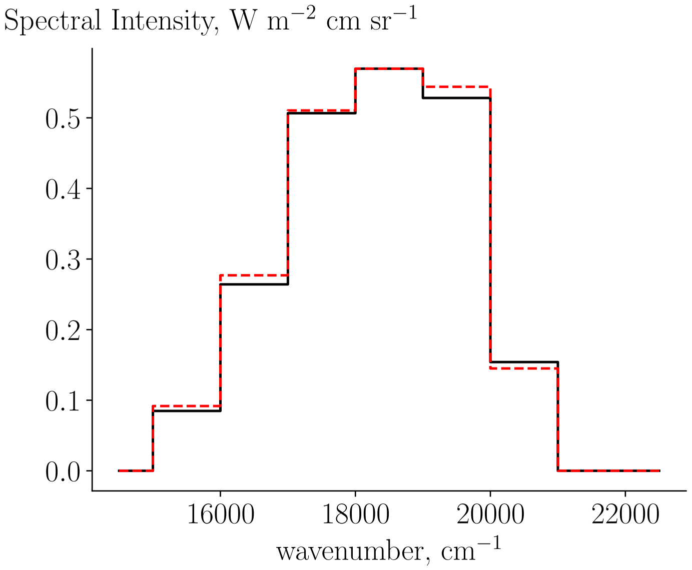

(c)

Fig. A.1: Verification of the narrowband properties of the filtered spectral intensity. (a) filter function in the visible range taken from Bessell (1990) and the corresponding narrowband average: —— $\overline{V_\sigma}^{\Delta\sigma}$, —— V_σ; (b) spectral intensity for air computed from Specair (Laux 2002) and the corresponding narrowband average: —— $\overline{I_\sigma}^{\Delta\sigma}$, - - - I_σ; (c) narrowband spectral intensity in the visible range; comparison of both side in Eq. A.4: —— $\overline{V_\sigma I_\sigma}^{\Delta\sigma}$, - - - $\overline{V_\sigma}^{\Delta\sigma} \cdot \overline{I_\sigma}^{\Delta\sigma}$

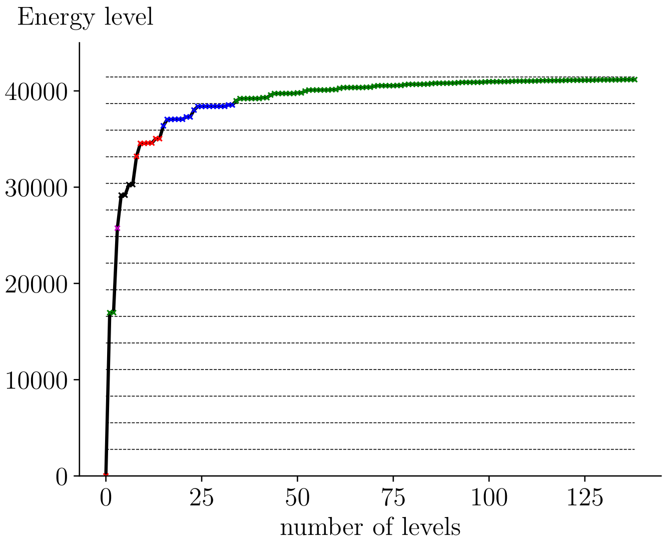

Fig. B.1: Energy levels for Na.

several atoms. Figure B.1 shows all 140 electronic levels for Na. The bars shown in the same figure represent the bins, and the symbols concern the total number of electronic levels per bin. The reduction technique mentioned above allowed us to pass from 140 to 6 electronic levels. The nodimensional enthalpy for Na is shown in B.2 for the total number of electronic levels extracted from Nist (Kramida & Ralchenko 1999) and for the reduced number.

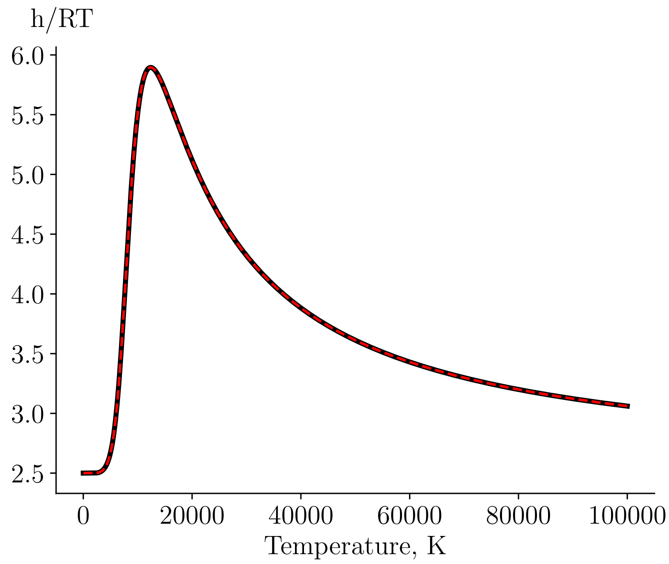

Fig. B.2: Nondimensional total enthalpy for Na; —— solid line: 140 electronic levels, - - - broken line: 6 electronic levels

From the figure, the agreement of the reduced system can reproduce the same thermodynamic quantity as the whole number of electronic levels. Finally, Fig. B.3 shows the equilibrium composition based on the Gibbs free energy minimization Scoggins & Magin (2015) for a Na elemental system. We compare the RRHO model and the Nasa polynomials database (McBride et al. February 2001), where the latter is more accurate up to 20000 K. Initially, only NaO is present in the mixture; around 2500 K, the species starts to dissociate, forming Na and O. Around 5000 K, Na starts to ionize, forming Na$^+$, and finally, at 12000 K, the mixture becomes fully ionized. The agreement between both models is excellent up to 17000 K, which corresponds to the limit of the Nasa polynomials for these species.

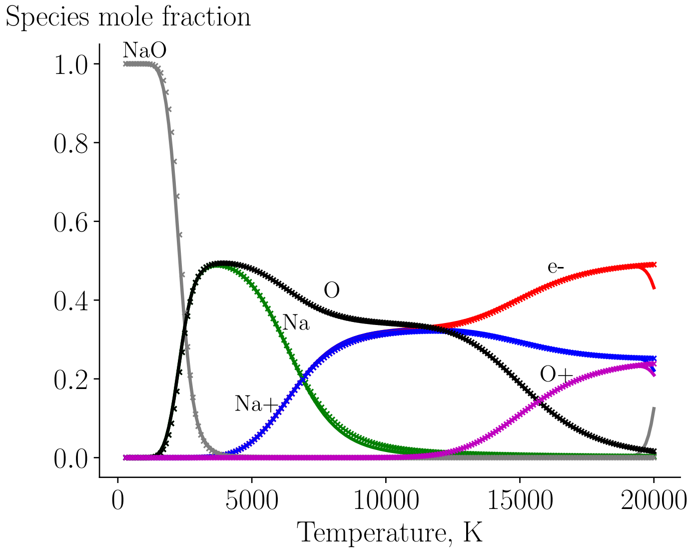

Fig. B.3: Equilibrium composition for {NaO, Na, O, Na$^+$, O$^+$, e$^-$}; lines: Nasa database, symbols: RRHO

Appendix B.2: Chemical reactions

Appendix B.3: Transport properties

Appendix B.4: Equilibrium vapor pressure

Table B.1: Arrhenius parameters for the gas-phase chemical reactions, $k_r^f(T_r^f) = AT_f^{\beta}\exp(-\theta/T_r^f)$

No.	Reaction	A m, s, mol	β	θ K	ref
	associative ionization ($T_r^f = T, T_r^b = T^{ve}$)				
1.	$\mathrm{N + O \rightleftharpoons NO^+ + e^-}$	5.30×10^{6}	0.00	31 900	1
2.	$\mathrm{O + O \rightleftharpoons O_2^+ + e^-}$	7.10×10^{-4}	2.70	80 600	2
3.	$\mathrm{N + N \rightleftharpoons N_2^+ + e^-}$	4.40×10^{1}	1.50	67 500	1
	charge exchange ($T_r^f = T, T_r^b = T$)				
4.	$\mathrm{NO^+ + O \rightleftharpoons N^+ + O_2}$	1.00×10^{6}	0.50	77 200	2
5.	$\mathrm{N^+ + N_2 \rightleftharpoons N_2^+ + N}$	1.00×10^{6}	0.50	12 200	2
6.	$\mathrm{O_2^+ + N \rightleftharpoons N^+ + O_2}$	8.70×10^{7}	0.14	28 600	2
7.	$\mathrm{O^+ + NO \rightleftharpoons N^+ + O_2}$	1.40×10^{-1}	1.90	26 600	2
8.	$\mathrm{O_2^+ + N_2 \rightleftharpoons N_2^+ + O_2}$	9.90×10^{6}	0.00	40 700	2
9.	$\mathrm{O_2^+ + O \rightleftharpoons O^+ + O_2}$	4.00×10^{6}	0.09	18 000	2
10.	$\mathrm{NO^+ + N \rightleftharpoons O^+ + N_2}$	3.40×10^{7}	−1.08	12 800	2
11.	$\mathrm{NO^+ + O_2 \rightleftharpoons O_2^+ + NO}$	2.40×10^{7}	0.41	32 600	2
12.	$\mathrm{NO^+ + O \rightleftharpoons O_2^+ + N}$	7.20×10^{7}	0.29	48 600	2
13.	$\mathrm{O^+ + N_2 \rightleftharpoons N_2^+ + O}$	9.10×10^{7}	0.36	22 800	2
14.	$\mathrm{NO^+ + N \rightleftharpoons N_2^+ + O}$	7.20×10^{7}	0.00	35 500	2
	electron impact dissociation ($T_r^f = T^{ve}, T_r^b = T^{ve}$)				
15.	$\mathrm{N_2 + e^- \rightleftharpoons N + N + e^-}$	3.00×10^{18}	−1.60	113 200	1
	heavy particle impact dissociation ($T_r^f = \sqrt{TT^{ve}}, T_r^b = T$)				
16.	$\mathrm{N_2 + M \rightleftharpoons N + N + M}$	7.00×10^{15}	−1.60	113 200	1
	M = N O	3.00×10^{16}			
17.	$\mathrm{O_2 + M \rightleftharpoons O + O + M}$	2.00×10^{15}	−1.50	59 360	1
	M = N O	1.00×10^{16}			
18.	$\mathrm{NO + M \rightleftharpoons N + O + M}$	5.00×10^{9}	0.00	75 500	1
	M = N O NO	1.00×10^{11}			
19.	$\mathrm{SiO + M \rightleftharpoons Si + O + M}$	4.00×10^{8}	0.00	95 600	3
20.	$\mathrm{SiO_2 + M \rightleftharpoons SiO + O + M}$	4.00×10^{8}	0.00	95 600	3
	exchange ($T_r^f = T, T_r^b = T$)				
21.	$\mathrm{NO + O \rightleftharpoons N + O_2}$	8.40×10^{6}	0.00	19 400	1
22.	$\mathrm{N_2 + O \rightleftharpoons NO + N}$	5.70×10^{6}	0.42	42 938	1
23.	$\mathrm{Si + NO \rightleftharpoons SiO + N}$	3.20×10^{7}	0.00	1775	4
24.	$\mathrm{Si + O_2 \rightleftharpoons SiO + O}$	2.10×10^{9}	−0.53	17	5
25.	$\mathrm{Fe + O_2 \rightleftharpoons FeO + O}$	1.3×10^{8}	0.0	10 200	6
26.	$\mathrm{Mg + O_2 \rightleftharpoons MgO + O}$	5.10×10^{4}	0.00	0	7
27.	$\mathrm{NaO + O \rightleftharpoons Na + O_2}$	2.20×10^{8}	0.00	0	8
28.	$\mathrm{Ca + O_2 \rightleftharpoons CaO + O}$	2.50×10^{8}	0.00	7250	9
	electron impact ionization ($T_r^f = T^{ve}, T_r^b = T^{ve}$)				
29.	$\mathrm{O + e^- \rightleftharpoons O^+ + e^- + e^-}$	3.90×10^{27}	−3.78	158 500	1
30.	$\mathrm{N + e^- \rightleftharpoons N^+ + e^- + e^-}$	2.50×10^{28}	−3.82	168 200	1
31.	$\mathrm{Na + e^- \rightleftharpoons Na^+ + e^- + e^-}$	2.50×10^{13}	−0.82	59 600	3
32.	$\mathrm{Fe + e^- \rightleftharpoons Fe^+ + e^- + e^-}$	2.50×10^{28}	−3.82	91 700	3
33.	$\mathrm{Mg + e^- \rightleftharpoons Mg^+ + e^- + e^-}$	2.50×10^{28}	−3.82	88 700	3
34.	$\mathrm{Ca + e^- \rightleftharpoons Ca^+ + e^- + e^-}$	2.50×10^{13}	−0.82	70 900	3
35.	$\mathrm{Si + e^- \rightleftharpoons Si^+ + e^- + e^-}$	2.50×10^{28}	−3.82	94 600	3

References. (1) Park et al. (2001); (2) Park (1993); (3) Johnston & Stern (2017); (4) Mick et al. (1993); (5) Le Picard et al. (2002) (6) Akhmadov et al. (1988); (7) Hodgson & Mackie (1979); (8) Plane & Husian (1986); (9) Kashireninov et al. (1977)

Table B.2: Parameters of the Lennard-Jones potential for neutral-neutral interaction

Species	Lennard-Jones Parameters			Polarizabilities	
	ϵ/k_b [K]	σ [Å]	ref	α [Å^3]	ref
Fe	7556	2.467	1	8.40	5
FeO	150	4.436	1	9.17	6
Mg	1614	2.926	2	10.6	5
MgO	150	4.454	1	11.37	6
Si	3036	2.91	2	5.38	5
SiO	569	3.374	2	6.15	6
SiO_2	2954	3.706	2	6.92	6
Na	1375	3.567	2	24.08	5
NaO	50	3.812	2	24.85	6
Ca	2954	4.517	1	22.8	5
CaO	100	4.650	1	23.57	6
K	850	4.250	1	43.4	5
N	119	2.98	3	1.10	7
N_2	71.4	3.798	4	1.74	7
NO	91.0	3.599	4	1.70	7
O	70.0	2.660	3	0.80	7
O_2	106.7	3.467	4	1.58	7

References. (1) McGee et al. (1998); (2) Svehla (1962); (3) Smith et al. (1999); (4) Park et al. (2001); (5) Lide (2004); (6) Lasaga & Cygan (1982); (7) Wright et al. (2007)

Table B.3: Equilibrium vapor pressure fit, $p_{\mathrm{vap},i}(T_w) = \exp(A - B/T_w)$

No.	Reaction	A	B
	standard boundary condition		
1.	$MgO(l) \rightleftharpoons Mg(g) + O(g)$	25.02	6.00×10^4
2.	$MgO(l) \rightleftharpoons MgO(g)$	28.28	7.38×10^4
3.	$Na_2O(l) \rightleftharpoons 2\,Na(g) + O(g)$	21.55	3.63×10^4
4.	$SiO_2(l) \rightleftharpoons Si(g) + 2\,O(g)$	31.17	1.06×10^5
5.	$SiO_2(l) \rightleftharpoons SiO(g)^+O(g)$	31.21	6.72×10^4
6.	$SiO_2(l) \rightleftharpoons SiO_2(g)$	27.98	6.65×10^4
7.	$FeO(l) \rightleftharpoons Fe(g) + O(g)$	23.67	5.16×10^4
8.	$FeO(l) \rightleftharpoons FeO(g)$	22.8	5.15×10^4
9.	$K_2O(l) \rightleftharpoons 2\,K(g)^+O(g)$	16.22	4.11×10^4
10.	$CaO(l) \rightleftharpoons Ca(g) + O(g)$	19.02	6.90×10^4
11.	$CaO(l) \rightleftharpoons CaO(g)$	22.71	8.18×10^4
	modified boundary condition		
1.	$MgO(l) \rightleftharpoons MgO(g)$	26.28	5.23×10^4
2.	$NaO(l) \rightleftharpoons NaO(g)^a$	23.12	5.23×10^4
3.	$SiO_2(l) \rightleftharpoons SiO_2(g)$	26.74	5.23×10^4
4.	$FeO(l) \rightleftharpoons FeO(g)$	25.52	5.23×10^4
5.	$KO(l) \rightleftharpoons KO(g)^a$	21.05	5.23×10^4
6.	$CaO(l) \rightleftharpoons CaO(g)$	23.65	5.23×10^4

Notes. (a) For simplicity Na_2O and K_2O were replaced respectively by NaO and KO. This change has a small impact on the flowfield because their concentration is much smaller than the other components (see Fig. 9d).